Bcl-xL enforces a slow-cycling state necessary for survival in the nutrient-deprived microenvironment of pancreatic cancer

Authors and affiliations: Yogev Sela[1,2,#], Jinyang Li[1,2,#], Shivahamy Maheswaran[1,2], Robert Norgard[1,2], Salina Yuan[1,2], Maimon Hubbi[1,2], Miriam Doepner[1], Jimmy P. Xu[3], Elaine Ho[3], Clementina Measaros[3], Colin Sheehan[4], Grace Croley[4], Alexander Muir[4], Ian A. Blair[3], Ophir Shalem[5,6], Chi V. Dang[7.8], Ben Z. Stanger[1,2*]

[1]Departments of Medicine and Cell and Developmental Biology, Perelman School of Medicine, University of Pennsylvania, Philadelphia, 19104, USA. [2]Abramson Family Cancer Research Institute, Perelman School of Medicine, University of Pennsylvania, Philadelphia, 19104, USA. [3]Department of Systems Pharmacology and Translational Therapeutics, Perelman School of Medicine, University of Pennsylvania, Philadelphia, 19104, USA. [4]Ben May Department of Cancer Research, University of Chicago, Chicago, IL 60637, USA. [5]Center for Cellular and Molecular Therapeutics, Children's Hospital of Philadelphia, Philadelphia, Pennsylvania 19104, USA. [6]Department of Genetics, Perelman School of Medicine, University of Pennsylvania, Philadelphia, Pennsylvania 19104, USA. [7]Systems and Computational Biology Center and Molecular and Cellular Oncogenesis Program, The Wistar Institute, Philadelphia, 19104, USA. [8]Ludwig Institute for Cancer Research, New York, 10016, USA.

[#]Both authors contributed equally to this work.

*Corresponding author: Ben Z. Stanger, Perelman School of Medicine, University of Pennsylvania, 421 Curie Blvd., Philadelphia, PA 19104. Phone: 215-746-5560. Email: bstanger@upenn.edu.

Contacts for reagent and resource sharing: Requests for information and reagents should be directed to the corresponding author (bstanger@upenn.edu).

Conflict of interest: B.Z.S. is a consultant for iTeos Pharmaceuticals and receives research funding from Boehringer Ingelheim Pharmaceuticals. I.A.B. is a consultant for Design Therapeutics, Calico Life Sciences, Chimerix Inc., Protypia, and the Takeda Pharmaceutical Company and receives research funding from the Takeda Pharmaceutical Company. C.V.D. is an advisor for Rafael Holdings, Inc., Barer Institute. All other authors declare no conflict of interest.

Keywords: Pancreatic cancer, Metabolism, Quiescence, CRISPR screening, BCL-xL

Running title: Dependencies of slow-cycling pancreatic tumor cells

Abstract

Solid tumors possess heterogeneous metabolic microenvironments where oxygen and nutrient availability are plentiful ('fertile regions') or scarce ('arid regions'). While cancer cells residing in fertile regions proliferate rapidly, most cancer cells in vivo reside in arid regions and exhibit a slow-cycling state that renders them chemoresistant. Here, we developed an in vitro system enabling systematic comparison between these populations via transcriptome analysis, metabolomic profiling, and whole-genome CRISPR screening. Metabolic deprivation led to pronounced transcriptional and metabolic reprogramming, resulting in decreased anabolic activities and distinct vulnerabilities. Reductions in anabolic, energy-consuming activities, particularly cell proliferation, were not simply byproducts of the metabolic challenge but rather essential adaptations. Mechanistically, Bcl-xL played a central role in the adaptation to nutrient and oxygen deprivation. In this setting, Bcl-xL protected quiescent cells from the lethal effects of cell cycle entry in the absence of adequate nutrients. Moreover, inhibition of Bcl-xL combined with traditional chemotherapy had a synergistic anti-tumor effect that targeted cycling cells. Bcl-xL expression was strongly associated with poor patient survival despite being confined to the slow-cycling fraction of human pancreatic cancer cells. These findings provide a rationale for combining traditional cancer therapies that target rapidly cycling cells with those that target quiescent, chemoresistant cells associated with nutrient and oxygen deprivation.

63 **Statement of Significance**

64 The majority of pancreatic cancer cells inhabit nutrient- and oxygen-poor tumor regions
65 and require Bcl-xL for their survival, providing a compelling anti-tumor metabolic
66 strategy.

67

Introduction

Uncontrolled proliferation is a hallmark of cancer, and thus most existing therapeutic strategies have been designed to target rapidly cycling cancer cells. However, the majority of cancer cells in solid tumors do not proliferate at any given time (1,2). The biology of these slow-cycling cancer cells is poorly characterized and rarely modeled despite the strong correlation between quiescence and therapy resistance (3,4). Filling this knowledge gap is critical, as a better understanding of the slow-cycling population of cancer cells could reveal new therapeutic opportunities, including drugs that could complement existing treatments.

The spatial distribution of rapidly and slowly cycling cells in solid tumors is not uniform. Rather, cancer cells exist in a continuum of metabolic microenvironments based on their proximity to patent blood vessels and nutrient access: a proximal (well-perfused) zone enriched for rapidly cycling tumor cells, an intermediate (poorly-perfused) zone dominated by viable slow-cycling cells, and a distal (non-perfused) zone with high levels of necrosis (5–7). Such metabolic zonation, characterized by varying levels of blood-borne nutrients and growth factors, likely dictate the proliferative and biosynthetic state of cancer cells (2,8,9).

Existing models of nutrient deprivation use cell culture conditions with a reduced abundance of specific nutrients including glucose, amino acids, growth factors, and oxygen (10,11), enabling the application of genetic screening (12–16). Whereas these studies have identified dependencies resulting from the absence of single or paired nutrients, cancer cells in poorly perfused regions of a tumor most likely suffer from the simultaneous deprivation of many nutrients and oxygen. This distinction is important

because tumor cells deprived of one nutrient can possibly survive through the utilization of other compensating metabolic pathways. Moreover, cells grown under most previously reported conditions continued to proliferate and thus do not fully model the slow-cycling and chemoresistant population.

Here, we established an *in vitro* experimental system to model the nutrient- and oxygen-deprived metabolic microenvironments of pancreatic tumors to understand how cancer cells adapt to comprehensive metabolic deficits. Through unbiased genetic screening, molecular profiling, and functional validation, we have identified vulnerabilities specific to metabolically deprived slow-cycling cancer cells and associated therapeutic opportunities.

Materials and Methods:

Cell culture

Human pancreatic and colorectal cancer cell lines were obtained from Anil Rustgi (University of Pennsylvania). MDA-MB-231 breast cancer cells were obtained from Andy Minn (University of Pennsylvania). Mouse MH6620c1 were previously isolated from late-stage primary tumors in C57BL/6 KPCY mice and generated by limiting dilution as described (17) and tested by the Research Animal Diagnostic Laboratory (RADIL) at the University of Missouri, using the Infectious Microbe PCR Amplification Test (IMPACT) II. Cultures were regularly tested using the MycoAlert Mycoplasma Detection Kit (Lonza,). Tumor cells were cultured under “fertile” or “arid” conditions using the following formulas:

Fertile conditions: Dulbecco’s modified Eagle’s medium (DMEM) (high glucose without sodium pyruvate) with 10% fetal bovine serum (FBS) (Gibco), glutamine (2 mM) and penicillin/streptomycin (1%) in 20% oxygen. Cells were passaged when 70-80% confluent.

Arid conditions: Basal media was prepared by dissolving 11g of DMEM without amino acids/glucose/pyruvic acid (D9800-26, US biological) into 1L of Distilled water (WFI grade) pH adjusted to 7.0-7.1. Basal media was mixed with DMEM containing amino acids without glucose/sodium pyruvate (Gibco) at a 1:4 ratio (to 20%) to which was added 0.5% fetal bovine serum (Gibco) 2.5mM glucose, 25mM HEPES (Gibco) 1% penicillin/streptomycin (Gibco), 0.2% Non-essential amino acids (Gibco), and 0.4 mM glutamine (Gibco). Cells were plated at 37,500 cells/cm^2 in all arid experiments and

cultured under 1% oxygen (Heracell 150i Thermo) with daily media replacement and without passaging.

Flow cytometry

Assessment of viability

For assessment of viability, media was collected from culture before harvest and combined with the pellet of the cells dissociated by trypsin. Cells were washed with PBS and Annexin staining buffer, stained with Annexin-V-APC (eBioscience) for 15 minutes, washed and incubated with propidium Iodide (PI) or DAPI as specified in each experiment.

EdU and OPP labeling *in vitro*

Tumor cells were pulsed with 10 μM EdU 24hrs before endpoint or 50 μM OPP 1hr before endpoint, followed by trypsinization, staining with Live/Dead Fixable Aqua stain kit (Thermo) and fixation with the FoxP3 transcription factor staining buffer set (eBioscience). Cells were then stained using the Click-iT reaction solution (100 mmol/L Tris-HCl pH 8.5, 4 mmol/L $CuSO_4$, 100 mmol/L ascorbic acid) for 30' at room temperature and analyzed by flow cytometry.

PKH proliferation kinetics assay

Tumor cells were trypsinized and stained with PKH26 (Sigma) or PKH67 (Sigma) according to the manufacturer's protocol. Briefly, cells were stained with dye for 3 minutes, washed with serum and seeded under fertile conditions. Tumor cells were sampled 24hrs later (t0) and cells were then cultured under fertile or arid conditions for

14-21 days depending on the experiment. Tumor cells were stained with DAPI and analyzed by flow cytometry at various timepoints to derive population doubling times.

Competition assays

Competition assays were performed by mixing EV cells and genetically modified cells at 1:1 ratio. Cells were sampled at day 0 by FACS to account for initial distributions and all subsequent measurements were normalized to day 0. For competition assays starting under arid conditions, PANC-1 cells expressing spCAS9 were transduced with sgBcl-xL-mCherry or non-targeting-mCherry vectors at a pre-calculated titer such that ~50% of the cells were transduced as determined by mCherry expression at day 4 post transduction by flow cytometry.

Pharmacological studies *in vitro*

For drug sensitivity assays, cells in the fertile culture were seeded on 12-well dishes at 18,000 cells/cm^2 and treated with selected drugs 24hrs later. The arid group was cultured for 0 (acute arid) or 14 (chronic arid) days under arid conditions prior to drug treatment. Cells supplemented daily for 4-5 days with fresh media supplemented with various drugs including: Gemcitabine (Pfizer), PHA-767491 (Cayman chemical), Silvestrol (Biovision), CPI-613 (Cayman chemical), UK 5099 (Cayman chemical) or A-1155463 (Cayman chemical) or vehicle (0.2% DMSO). Tumor cells were fixed at day 0 or endpoint (day 4-5) with paraformaldehyde 4% stained with 3 μM Hoecsht 33342 (Thermo) for 30' at 37C and quantified using a fluorescence plate reader (Molecular devices) to assess cell numbers. Cell density was normalized for day 0 of each group.

For pharmacological inhibition of biosynthesis under serum repletion, treatment initiated with switch to arid conditions (acute arid) and cells were treated for 72hrs before readouts. Drugs used in that study include: Abemacicilib (MedChem Express), Rapamycin (ApexBio), Torin1 (MedChem Express) and Cycloheximide (Sigma).

CRISPR-Cas9 screen

Cas9 was introduced to the PANC-1 cell line by transduction of the lentiCas9-Puro construct (Addgene plasmid #52962), and selected with 10μg/mL blasticidin. 320 million Cas9 expressing cells were transduced with the Brunello sgRNA library (18) at a MOI of 0.3 such that ~30% of cells were puromycin resistant yielding 300x coverage of the sgRNA library. T0 samples were collected by FACS 3 days post-transduction. Cells were selected under fertile conditions in the presence of puromycin 2μg/ml for additional 5 days to achieve complete puromycin selection and cultures were separated for culture under fertile or arid conditions as described above (See results section). Genomic DNA from half of the cell pellets representing 150x coverage was processed for library generation. DNA was extracted by incubation with NK lysis Buffer (50 mM Tris, 50 mM EDTA, 1% SDS, pH 8) and 20 mg/ml Proteinase K (Qiagen 19131) at 55 °C overnight, followed by incubation with 10 mg/ml RNAse A (Qiagen 19101) at 37 °C for 30 minutes and protein precipitation using 7.5M ammonium acetate (Sigma A1542). Precipitate was vortexed and then centrifuged at ≥ 4,000 x g for 10 minutes, washed with 100% isopropanol, and 70% ethanol and the pellet was air dried and resuspended in 1x TE buffer (Sigma T9285).Libraries were constructed according to previously described protocols (19). Briefly, sgRNAs were amplified over 24 cycles with Herculase II fusion DNA polymerase (Agilent) per

manufacturer specifications with PCR#1 forward and reverse primers. Each reaction included 5µg of genomic DNA, and multiple PCR reactions were run in parallel such that all extracted genomic DNA was used to maintain library coverage. PCR reactions were then pooled for each sample, and 5 µl of each pooled PCR#1 sample was used as a template for PCR#2, which added Illumina P5/P7 adapters, barcodes, and staggers for nucleotide complexity. For PCR#2, template was amplified over 7 cycles with PCR#2 forward and reverse primers, and the resulting reactants were column purified with the QIAquick PCR purification kit (Qiagen) and gel extracted with the QIAquick gel extraction kit (Qiagen). The barcoded libraries were then pooled at an equal molar ratio and sequenced on a NextSeq500/550 sequencer (Illumina, 150 cycles High Output kit v2.0) to generate 150 bp single end reads. MAGeCK software was used for analysis. Briefly, the resulted sequencing data were de-barcoded, merged, and the 20 bp sgRNA sequence was aligned to the reference sgRNA library without allowing for any mismatches. The read counts were calculated for each sgRNA with normalization to the non-targeting sgRNAs. Differential analysis of sgRNA and targeted genes was done following the MAGeCK pipeline with standard parameters. Pathway analysis of identified genes were done using EnrichR (https://maayanlab.cloud/Enrichr/). Detailed Scripts and parameters used for each step of analysis could be provided by request to the authors.

Primers used for library preparation:

PCR #1 forward	AATGGACTATCATATGCTTACCGTAACTTGAAAGTATTTCG
PCR #1 reverse	CTTTAGTTTGTATGTCTGTTGCTATTATGTCTACTATTCTTTCC

Note: italicized = stagger sequence; bold = barcode sequence

Sample	**PCR #2 forward primer sequence**
d0	AATGATACGGCGACCACCGAGATCTACACTCTTTCCCTACACGACGCTCTT

	CCGATCT*ACGATCGAT***TCCTTGGT**TCTTGTGGAAAGGACGAAACACCG
d9 fertile	AATGATACGGCGACCACCGAGATCTACACTCTTTCCCTACACGACGCTCTT CCGATCT*T***ACAGGTAT**TCTTGTGGAAAGGACGAAACACCG
d30 arid	AATGATACGGCGACCACCGAGATCTACACTCTTTCCCTACACGACGCTCTT CCGATCT*AT***CTAACTCG**TCTTGTGGAAAGGACGAAACACCG
d30 fertile	AATGATACGGCGACCACCGAGATCTACACTCTTTCCCTACACGACGCTCTT CCGATCT*GAT***AACAATGG**TCTTGTGGAAAGGACGAAACACCG
d32 fertile	AATGATACGGCGACCACCGAGATCTACACTCTTTCCCTACACGACGCTCTT CCGATCT*CGAT***ACTGTATC**TCTTGTGGAAAGGACGAAACACCG
d53 arid	AATGATACGGCGACCACCGAGATCTACACTCTTTCCCTACACGACGCTCTT CCGATCT*TCGAT***AGGTCGCA**TCTTGTGGAAAGGACGAAACACCG
d53 fertile	AATGATACGGCGACCACCGAGATCTACACTCTTTCCCTACACGACGCTCTT CCGATCT*CGATCGAT***CCAACATT**TCTTGTGGAAAGGACGAAACACCG

214

PCR #2 reverse primer sequence
CAAGCAGAAGACGGCATACGAGATGTGACTGGAGTTCAGACGTGTGCTCTTCCGATCT TCTACTATTCTTTCCCCTGCACTGT

215

216 Processed read counts from the CRISPR screen are presented in Table S1.

217

218 **RNA-seq analysis**

219 RNA samples were extracted using the Qiagen RNeasy Kit, following manufacturer's
220 instructions. RNA samples were sent for library preparation and next generation
221 sequencing by Novogene (California, USA). Raw counts of gene transcripts were derived
222 from fastq files using an alignment-independent quantification tool, Salmon
223 (https://combine-lab.github.io/salmon/), with standard settings. The raw count matrix was
224 then imported into R-studio and utilized as input for DESeq2 analysis for normalization,
225 differential gene expression analysis, and principal component analysis. The output of
226 DESeq2 was used as the input for pre-ranked based GSEA for enrichment of functional
227 pathways and gene signatures (https://www.gsea-msigdb.org/gsea/index.jsp). Detailed
228 Scripts and parameters used for each step of analysis can be provided by the authors upon
229 request.

Expression analysis and overall survival analysis in human samples

Analysis of the expression of *BCL2L1* across different types of cancer and normal tissues, and correlation with overall survival, was done using an online tool, Gene Expression Profiling Interactive Analysis (GEPIA) (http://gepia.cancer-pku.cn/). Analysis of the expression of *BCL2L1* in proliferating and quiescent cancer cells using published single cell RNA-seq datasets of human pancreatic cancer samples was done using Seurat (https://satijalab.org/seurat/). The output of Seurat-based differential gene expression analysis was used as the input for pre-ranked based GSEA for enrichment of functional pathways and gene signatures (https://www.gsea-msigdb.org/gsea/index.jsp). Detailed Scripts and parameters used for each step of analysis can be provided by the authors upon request.

Metabolomics

Metabolomic Extraction

Metabolomic extraction from cells was done as described (20) et al. 1 mL of cold 80% MeOH from -80˚C, 40 µL of Metabolomics ISTD mix were added to each plate (Table S2). Cells were scraped and transferred to microcentrifuge tubes in ice. Samples were pulse-sonicated in ice with a sonic dismembranator (Fisher Scientific, Waltham, MA) for 30 sec, incubated on ice for 10 min, and then pulsed again for 30 sec. Samples were pelleted by centrifugation at 6000 x *g* for 5 min at room temperature. 500 µL of supernatant was moved to a clean microcentrifuge tube, dried under nitrogen, and

resuspended in 50 µL of 5% (w/v) SSA in water. 3 µL injections were used for LC-HRMS analysis.

Metabolomic LC-HRMS

Metabolites were separated using a XSelect HSS C18 column (2.1 mm x 150 mm, 3.5 µm particle size) (Waters, Milford, MA) in an UltiMate 3000 quaternary UHPLC (Thermo Scientific, Waltham, MA) equipped with a refrigerated autosampler (5^{o}C) and column heater (50^{o}C). Solvent A consisted of water with 5 mM DIPEA and 200 mM HFIP and Solvent B consisted of MeOH with 5 mM DIPEA and 200 mM HFIP. Flow gradient conditions were as follows: 0% B for 6 min at 0.18 mL min^{-1}, increased to 1% B for 2 min at 0.2 mL min^{-1}, increased to 2% B for 4 min, increased to 14% B for 2 min, increased to 70% B for 2 min, increased to 99% B for 1 min, increased flow rate to 0.3 mL min^{-1} for 0.5 min, increased flow rate to 0.4 mL min^{-1} for 4 min, then washed by decreasing to 0% B for 2.3 min at 0.3 mL min^{-1}, decreased to 0.2 mL min^{-1} for 0.2 min, and ending with flow of 0.18 mL min^{-1}. Samples were analyzed using a Q Exactive HF (QE-HF) (Thermo Scientific, Waltham, MA) equipped with a heated electro-spray ionization (HESI) source operated in the negative ion mode as described by Frederick et al. Column effluent was diverted to the QE-HF from 0.5 to 19 min and then to waste for the remaining time of the run.

Timelapse microscopy

PANC-1 WT and Bcl-xL KO cells tagged with the FUCCI-PIP reporter (Addgene #138715, (21) were seeded on 12-well plates (Falcon), cultured under arid conditions for 48hrs and imaged for additional 48hrs hours via EVOS Auto FL2 microscope

(ThermoFisher) under 1% or 20% oxygen and images acquired hourly. Time-lapse movies were constructed via ImageJ and quantification of cell cycle transitions and cell death was done manually.

ATP measurements

For ATP measurements, 10,000 tumor cells were seeded in parallel on standard (for cell numbers) or opaque (for ATP) 96 well plates and cultured under fertile or arid condition for 3 or 14 days. ATP was then assessed using CellTiter-Glo (Promega) and cell numbers were quantified by Hoechst 33342 staining as described above to derive ATP/cell ratios.

Western blots

Cells were washed with ice-cold phosphate-buffered saline (PBS) and lysed in RIPA buffer (Cell signaling technology). Equal amounts of protein were run in reducing conditions on 4–20% Mini-PROTEAN gels (Bio-Rad) and transferred to Immun-Blot PVDF Membrane (Bio-Rad). Blocking was performed in 5% non-fat dry milk for 1 hour at room temperature. After blocking, membranes were incubated in primary antibody diluted in 5% non-fat dry milk overnight at 4°C. After PBS-T washes, membranes were incubated with secondary antibody diluted in 5% non-fat dry milk at room temperature for 1 hour. Following PBS-T washes, membranes were soaked in ECL or ECL plus (Pierce) kits depending on the target and imaged with Chemi-doc imaging system (Bio-Rad). Antibodies used: Monoclonal mouse S6 1:1000 (Cell signaling technology, 2317S), Polyclonal Rabbit Phospho S6 Ribosomal Protein (Ser235/236) 1:1000 (Cell

signaling technology 2211S), Monoclonal mouse α-tubulin 1:5000 (Cell signaling technology 3873S, c-myc, Rabbit polyclonal Bcl-xL 1:1000 (Proteintech 10783-1-AP), Rabbit polyclonal 1:1000 Mcl-1 (Proteintech 16225-1-AP).

Immunofluorescence and microscopy

Tissue processing and Immunohistochemistry

Tumors were fixed by 4% paraformaldehyde for 24hrs, followed by incubation in 30% sucrose for 24hrs, embedding in OCT and freezing on dry ice. Frozen sections (7μm) were obtained using a cryostat (Leica) and stored at -80C. For staining, sections were thawed, blocked in 0.3% triton-X with 5% normal donkey serum for 1hr, incubated overnight with rat monoclonal Ki-67 (ebiosciences,1:100), rabbit polyclonal cleaved caspase 3 antibody (Cell signaling technology,1:200), rabbit G0S (Proteintech 1:100), rabbit FABPS (Proteintech 1:100)or rabbit UPAR (Proteintech 1:400) in 5% donkey serum in PBST 0.1%. Sections were then washed, incubated with secondary antibodies and DAPI for 1hr and mounted. For EdU staining, samples were permeabilized with 0.5% Triton-X for 20 minutes, washed and incubated with buffer containing 100 mmol/L Tris-HCl pH 8.5, 8 mmol/L $CuSO_4$, and 100 mmol/L ascorbic acid for 30' at room temperature followed by immunostaining as described. Whole-tumor sections were visualized using a LSM710 equipped with a X20 objective and robotic stage. Images were quantified using ImageJ. To calculate distance from perfused blood vessels, dextran pixels were thresholded to create a 32-bit EDM map. For each analysis, pixels of choice (e.g GFP+, mCherry+, GFP+CC+ pixels etc.) were thresholded and overlaid on EDM maps to derive spatial histograms of each type of pixel. Percentages of Ki-67+

and CC3+ pixels in tumor cells was defined as the ratio of co-localizing pixels (Ki-67 or CC3)/total tumor pixels derived from spatial histograms.

Immunocytochemistry

Tumor cells were fixed with 4% paraformaldehyde for 15', blocked with 5% donkey serum for 1hr and stained overnight at 4C with Ki-67 (eBioscience, 1:100) or rabbit polyclonal phospho-S6 (Cell Signaling Technology 1:400) in 5% donkey serum in PBST 0.1%, stained with secondary antibody and DAPI and imaged by EVOS Auto FL2 microscope (ThermoFisher)

Lentivirus transduction of tumor cells for CRISPR-mediated ablation

Cell lines were first transduced with Lentspicas9-puro (Addgene plasmid #108100; (22)) or Lenti-v2-cas9-GFP (Addgene plasmid #82416; (23)). sgRNAs were cloned into LRGFP (Addgene plasmid #65656; (24)) or LRmcherry (a gift from Shi Junwei). Tumor cells modified to expressed spCas9 were transduced with sgRNAs derived from the following primer sequences:

Target gene	Forward primer	Reverse primer
Human TSC2-1	caccgCAGCATCTCATACACACGCG	aaacCGCGTGTGTATGAGATGCTGc
Human TSC2-2	caccgCCTCTACAGGAACTTTGCCG	aaacCGGCAAAGTTCCTGTAGAGGc
Human Bcl-xL1	caccgCAGGCGACGAGTTTGAACTG	aaacCAGTTCAAACTCGTCGCCTGc
Human Bcl-xL2	caccgGACCCCAGTTTACCCCATCC	aaacGGATGGGGTAAACTGGGGTCc
Mouse Bcl-xL	caccgAGTAAACTGGGGTCGCATCG	aaacCACATGTGTGCTAGGATCAGc
Non-targeting	caccgGCTTGAGCACATACGCGAAT	aaacATTCGCGTATGTGCTCAAGCc

All lentiviral and retroviral vectors were transfected into 293T cells using 1mg/ml PEI, and virus was harvested 48hrs and 72hrs later. Viral particles were transduced into cells using 4ug/ml polybrene.

340

341 **Autophagy**

342 PANC-1 cells were transduced with a pBABE-puro mCherry-EGFP-L3CB (Addgene
343 plasmid #22418; (25)). At day 14, tumor cells were analyzed by flow cytometry and the
344 ratio of mCherry/GFP fluorescence was measured.

345

346 **Macropinocytosis**.

347 PANC-1 cells were seeded onto glass coverslips and grown under fertile conditions for
348 24hours or arid conditions for 14 days. Media was then switched to arid media
349 containing 1mg/ml TMR-dextran (D1818, Invitrogen) for 30 minutes at 37°C. At the end
350 of the incubation period, cells were rinsed five times in cold PBS and immediately fixed
351 in 3.7% formaldehyde. Cells were DAPI-treated to stain nuclei and coverslips mounted
352 onto slides using Aquamount (Thermo). Images (x63 oil lense,0.7µm optical-sections)
353 were captured by confocal microscopy using a LSM880 (Zeiss) and analyzed using the
354 'Analyze Particles' feature in ImageJ (NIH). 3 fields were analyzed for each
355 experimental group in each experiment.

356

357 **Animal studies**

358 $Kras^{LSL\text{-}G12D}$; $p53^{L/+}$; Pdx1-cre; $Rosa26^{YFP/YFP}$ (KPCY) mice have been described
359 previously. 6- to 8-week-old C57BL/6J (male) or NOD.SCID (male and female) mice
360 were purchased from The Jackson Laboratories and Charles River Laboratories,
361 respectively, for tumor cell injection experiments. All vertebrate animal experiments
362 were conducted in compliance with the National Institutes of Health guidelines for

363 animal research and approved by the University of Pennsylvania Institutional Animal
364 Care and Use Committee (IACUC).

365 Evaluation of proliferation in differentially perfused regions

366 To estimate proliferation and cell death in differentially perfused regions, mice bearing
367 KPCY tumors (~10mm in diameter) were injected 4 times with 10mg/kg EdU over a
368 period of 48 hours in 12-hour intervals. Mice were injected with 70 kDa TMR-dextran
369 (Invitrogen) 30 minutes prior to sacrifice and 2 different sections per mouse, 5 well-
370 perfused and 5 poorly perfused regions were evaluated for proliferation and apoptotic
371 markers by manual counting of YFP+ cells.

372 Establishment and evaluation of tumor xenografts

373 Cells containing EV-GFP and Bcl-xL KO-mCherry clones $8x10^6$ cells in DMEM were
374 inoculated into the flanks of NOD.SCID mice (males and females) and tumor size was
375 measured by calipers starting 6 weeks post implantation. Proliferation and cell death
376 were measured in 2 separate sections per mouse.

377 Competition assay in vivo

378 EV-GFP and Bcl-xL KO-mCherry cells (non-clonal) were mixed at a 1:1 ratio 24hr
379 before implantation and proportions were confirmed by flow cytometry. A mixture
380 containing $8x10^6$ cells in DMEM was inoculated into the flanks of NOD.SCID mice
381 (males and females) and harvested when tumors reached 7-9mm in diameter. TMR-
382 dextran 70 kDa was injected retro-orbitally 30 minutes prior to sacrifice. For each
383 mouse, 2 sections representing different regions of the tumor were analyzed for relative
384 thresholded area and spatial distribution (relative to dextran signal) of EV-GFP and Bcl-
385 xL KO-mCherry cells.

Intra-tumoral injections

PANC-1-GFP xenografts were established by injection of $8x10^6$ cells in DMEM into the flanks of male or female NOD.SCID mice. Tumors were allowed to grow to 7-9mm in diameter and then injected intratumorally using a 27g needle with 50µl with either PBS, A-1155463 (Cayman chemical, 1.25mg/ml) in buffer containing 10% DMSO, 40% PEG300, 5%l T80, 45% Saline, Buffer alone Gemcitabine (Pfizer, 1mg/ml) + albumin-conjugated paclitaxel (Abraxis, 0.6mg/ml) at a rate of ~50µl/minute. 24 hours post injection, Texas red-dextran 70 kDa was injected retro-orbitally 30 minutes prior to sacrifice. 4-6 sections per mouse (from different regions) were evaluated for apoptosis rates in GFP+ cells.

Long term drug treatment

MH6620c1 subcutaneous tumors were established by inoculation of $3x10^5$ cells in DMEM to the flanks of C57BL/6J male mice and allowed to grow to 6-9mm. Mice were then randomly assigned to one of four groups receiving the following treatments: 120mg/kg Gemcitabine (Pfizer) + 120mg/kg Nab-Paclitaxel (Abraxis) twice-weekly intraperitoneally, 10mg/kg of A-1331852 ChemieTek) in buffer containing 10% ETOH, 27.5% PEG400 and 60% Phosal 50G by oral gavage, Combined chemotherapy+ A-1331852, A-1331852 buffer alone by gavage+PBS injection. Tumor size was measured by calipers.

Statistical analysis

Comparisons between two groups were performed using Students' unpaired t test. One way ANOVA with Dunnett, Holm Sidak, corrections for multiple testing was applied as

described for each analysis. All statistical analyses were performed with Graphpad Prism 9 (GraphPad). Error bars show standard error of the mean (SEM) unless otherwise indicated., and $p<0.05$ was considered statistically significant. * indicates $p<0.05$, ** $p<0.01$, *** $p<0.001$, and **** $p<0.0001$. ns denotes not significant. For sequencing experiments, DESeq2 (26)) was used to generate adjusted p-values (FDR). For TCGA survival analysis, KM plotter (27) was used to generate logrank P-values.

Data Availability Statement

The data generated in this study are publicly available in Gene Expression Omnibus (GEO) under the accession number GSE176076 or are available within the article and its supplementary data files.

Results

Modeling metabolic heterogeneity in pancreatic cancer

Pancreatic ductal adenocarcinoma (PDAC) is a highly nutrient-depleted and hypoxic tumor type due to its dense stroma and low vascularity (28–31). As a result, most PDAC cancer cells cycle slowly *in vivo* (32–35). The altered metabolic milieu within tumors (36) stands in contrast to standard culture conditions, where PDAC cancer cells have access to supraphysiological quantities of amino acids, sugars, lipids, oxygen, and growth factors and exhibit a high proliferative index. We therefore hypothesized that the low proliferation rate of cancer cells *in vivo* reflects a reduced availability of blood-borne oxygen and nutrients. To test this, we introduced 70 kDa Texas Red-conjugated dextran into autochthonous pancreatic tumor-bearing KPCY animals (32) by intravenous (IV) injection and measured red fluorescence as a surrogate for perfusion (Fig. S1A). We then identified regions that were dextran-high ("well perfused") or dextran-low ("poorly perfused") (see Methods) and compared rates of tumor cell proliferation by measuring 5-ethynyl-2'-deoxyuridine (EdU) incorporation and Ki-67+ staining in YFP+ cancer cells. As expected, cancer cells in well-perfused areas exhibited a significantly higher rate of proliferation (Fig. 1A, B and Fig. S1B). By contrast, rates of apoptosis, as measured by staining for cleaved caspase-3 (CC3), were not different between well-perfused and poorly perfused regions (Fig. 1A, B). These results are consistent with the notion that pancreatic tumors are metabolically heterogeneous (37), and that cancer cells in poorly perfused regions acquire a slow-cycling, viable state.

To establish an *in vitro* experimental system that recapitulates the quiescent state associated with nutrient poor, hypoxic conditions *in vivo*, we varied media

composition and oxygen concentrations to identify conditions that resulted in a significant reduction in cell proliferation without loss of cell viability (Fig. S1C,D). Using PANC-1 cells, we found that DMEM supplemented with 2.5 mM glucose, 0.5% fetal bovine serum (FBS), and 20% of standard amino acid concentration fulfilled this goal when cells were grown at an oxygen concentration of 1% (Fig. 1C), noting that this does not necessarily mimic *in vivo* conditions. Under these "arid" conditions, cells had reduced DNA synthesis (Fig. 1D) but no increase in cell death (Fig. 1E) as compared to cells grown under standard "fertile" conditions (DMEM with 25 mM glucose, 10% fetal bovine serum, 100% amino acids, 20% oxygen). Cell labeling with PKH26, a fluorescent dye that is diluted with each round of cell division, indicated a dramatic change in doubling time associated with the transition to arid conditions, increasing nearly 5-fold after 7d and nearly 18-fold after 21d (Fig. 1F and Fig. S1E). Importantly, slow-cycling cancer cells resumed normal proliferation after a return to fertile conditions, indicating that they had not entered an irreversible growth arrested state (Fig. 1F). Similar results were obtained with a KPCY-derived mouse cell line, MH6620c1 (17) (Fig. S1F-H).

Next, we assessed the effect of arid conditions on other metabolic phenotypes. Consistent with prior studies (38–40), nutrient and oxygen deprivation prompted a significant decrease in protein synthesis measured by O-propargyl-Puromycin (OPP) incorporation (Fig. 1G) as well as a significant increase in metabolic scavenging pathways, including autophagy and macropinocytosis (Fig. 1H-I). These changes were associated with a decrease in cell size (Fig. S1I). As expected, steady-state metabolomics of cells grown for 7-14 days under arid condition revealed a depletion of TCA cycle intermediates and most acyl-CoAs as well as a reduction in intracellular

amino acid pools (Fig. S2A-B and Table S1). These changes in metabolite levels were associated with a ~50% reduction in intracellular ATP (Fig. 1J). These results indicate that combined nutrient and oxygen deprivation results in a severe depletion of intracellular biofuels and a hypo-energetic state.

Cells grown under arid conditions for 2 days exhibited dramatic changes in gene expression, with 3196 genes upregulated and 2687 genes downregulated ($p_{adj} < 0.05$) compared to cells grown under fertile conditions (Fig. S3A). Functional annotation by gene set enrichment analysis (GSEA) revealed the hypoxia-HIF response to be the most highly induced gene set, with related stress responses including glycolysis, autophagy, NFκB, and cell cycle inhibitory pathways also exhibiting upregulation (Fig. S3B). Oxidative phosphorylation and pathways associated with proliferation, such as targets of MYC and E2F, dominated the transcriptional profile of genes downregulated under arid conditions (Fig. S3C). Components of the TCA cycle and the electron transport chain were also down regulated (Fig. S3D), as were genes involved in nucleic acid and protein synthesis (Fig. S3E). These results indicate that adaptation to arid conditions is associated with widespread transcriptional reprogramming, resulting in the induction of glycolytic and autophagic pathways and repression of TCA cycle and biosynthetic pathways. To confirm that the gene expression changes associated with arid adaptation *in vitro* is consistent with regulatory events occurring *in vivo*, we stained tumors for three proteins whose mRNA levels decreased under arid conditions (Fig. S4A). All three exhibited the expected expression pattern *in vivo* – high in perfusion-proximal regions and low in perfusion-distal regions (Fig. S4B) – suggesting that arid

conditions model at least some of the adaptations experienced by cells in poorly perfused regions of the tumor.

Finally, to determine whether the slow-cycling state impacts sensitivity to chemotherapy, we examined the dose-response of PANC-1 cells to Gemcitabine. Under fertile conditions, cells were sensitive at an IC_{50} of 16.63 μM, similar to previous findings (41) (Fig. 1K). By contrast, cells grown under arid conditions were fully resistant to Gemcitabine, even at a dose of 1 mM (Fig. 1K) as expected based on Gemcitabine's activity as an inhibitor of DNA synthesis. These results suggest that metabolically deprived slow-cycling tumor cells represent a chemoresistant subpopulation, a result we later confirmed *in vivo* (see below).

CRISPR screening identifies genes that are either essential for, or detrimental to, adaptation to arid conditions

We hypothesized that cellular adaptations to metabolic deprivation might be associated with selective (and exploitable) gene dependencies. To identify such dependencies, we performed a genome-wide CRISPR screen utilizing Cas9-expressing PANC-1 cells and the Brunello sgRNA library, which targets over 19,000 genes (18). Cancer cells were first allowed to grow in fertile medium to allow short- or long-term depletion of sgRNAs targeting genes required for cell viability under standard culture conditions. At day 9 and day 32 after transduction (denoted as early and late fertile references points), transduced cells were sub-cultured and propagated under arid conditions or fertile conditions for an additional 21 days. Genomic DNA was extracted 3 days after transduction to account for library representation (T_0), at early and late

513 reference points (d9 fertile, d32 fertile), and at both 21-day endpoints (d30 arid, d30
514 fertile; d53 arid, and d53 fertile) (Fig. 2A).

515 We first sought to determine which genes and pathways are essential under
516 fertile conditions but not arid conditions. As expected, such genes were predominantly
517 associated with cell growth programs including cell cycle progression and biosynthesis
518 (Fig. S5A and Table S2-S3). For example, sgRNAs targeting genes regulating cell
519 proliferation (e.g., MYC, DBF4, and CCNB1) or translation (e.g., EIF4A1, RPL12, and
520 RPL5) were depleted prior to the early reference point and further depleted following an
521 additional 21 days of culture under fertile conditions (Fig. 2B, compare d9 fertile to d30
522 fertile). By contrast, there was little selection against these genes following transfer to
523 arid conditions (Fig. 2B, compare d9 fertile to d30 arid). These results confirm that this
524 screening approach identifies differential genetic dependencies of cells grown under
525 fertile vs. arid conditions.

526 We next performed the reciprocal analysis to identify genes and pathways
527 necessary under arid conditions but not fertile conditions. This was achieved by
528 identifying sgRNAs that are depleted in both early (d30) and late (d53) arid conditions
529 but not under any fertile conditions. Unfiltered functional annotation of genes targeted
530 by these sgRNAs revealed an association with components of the electron transport
531 chain and the TCA cycle (Fig. 2C). For example, sgRNAs targeting components of
532 mitochondrial complex I (e.g. NDUFB10, NDUFC1, and UQCC1) or the TCA cycle (e.g.
533 MDH2, MPC1, and SUCLG1) were among the top hits depleted under arid conditions,
534 whereas there was little selection under fertile conditions (Fig. 2D, compare d32
535 reference to d53 arid vs. fertile; Fig S4C,D; Tables S2-3). As arid conditions induce a

slow-cycling state, the observed dependencies likely reflect a requirement for cell survival rather than a requirement for cell growth and proliferation.

To confirm the vulnerabilities identified in our CRISPR screen, we measured the sensitivity of cells grown under arid or fertile conditions to a panel of small molecule inhibitors. In agreement with our observations from gemcitabine treatment (Fig. 1F), inhibitors targeting the cell cycle regulator DBF4 (PHA767491, (42)) or the translation initiation factor EIF4A1 (Silvestrol, (43)) caused a dose-dependent growth arrest of PANC-1 cells under fertile conditions but had little effect under arid conditions (Fig. S5B). Conversely, cells grown under arid conditions were highly sensitive to inhibitors targeting the TCA cycle such as devimistat (CPI-613) (44) or the mitochondrial pyruvate carrier MPC1 such as 2-cyano-3-(1-phenyl-1H-indol-3-yl)-2-propenoic acid (UK-5099) (45), whereas these drugs had no effect on the survival of cells grown under fertile conditions, even at high micromolar concentrations (Fig. 2E). Similar drug response profiles were observed in AsPC-1 and HPAC cells (Fig. S5C,D).

Because arid conditions prompted a reduction in DNA and protein synthesis (Fig. 1D, Fig. 1G, and Fig. S3), we hypothesized that anabolic processes might be detrimental to cell survival during nutrient and oxygen deprivation. To this end, we re-examined our CRISPR data for sgRNAs that were enriched, rather than depleted, under arid but not fertile conditions. Functional annotation indicated an enrichment for target genes involved in cell cycle progression and biosynthesis as well as targets of the PRC2 complex (Fig. 2F). Conversely, sgRNA targeting several genes that suppress biosynthesis were depleted under arid conditions (Tables S2-S3) including tuberous sclerosis 2 (TSC2). TSC2 is a negative regulator of the mammalian target of rapamycin

559 (mTOR), a master regulator of cell growth (46), and thus its loss would be expected to
560 trigger inappropriate growth and proliferation under metabolically adverse conditions. To
561 test this hypothesis, we generated PANC-1 cell lines lacking TSC2 and confirmed that
562 this resulted in an acute increase in DNA and protein synthesis (Fig. 2G-H) and mTOR
563 activity as measured by S6 phosphorylation (Fig. 2I). We then performed a competition
564 experiment in which we mixed wild-type (WT) cells (GFP+) with TSC2-deficient cells
565 (mCherry+) at a 1:1 ratio and cultured them under fertile or arid conditions for 7, 14, or
566 21 days. As shown in Fig. 2J, TSC2 wild-type cells out-competed TSC2-deficient cells
567 under arid conditions, while there was minimal difference under fertile conditions. This
568 decrease in TSC2-deficient cell fitness was attributable to a loss of viability under arid
569 but not fertile conditions (Fig. S5E,F). Thus, loss of the TSC2 tumor suppressor leads to
570 a paradoxical reduction in the fitness of metabolically deprived cells, in line with its
571 protective role against hypoxia-induced energy stress (46).

572 Taken together, these results indicate that certain pathways sustain cell survival
573 under arid conditions while other pathways hinder survival. The first category consists of
574 genes involved in the TCA cycle and OXPHOS, which may reflect a heightened
575 dependency on ATP production or other metabolites generated by these pathways. The
576 second category consists of genes involved in negative control of growth and
577 proliferation, suggesting that enforced biosynthesis in the absence of adequate nutrient
578 and oxygen availability is detrimental for cell survival. Hence, the reduction in anabolic
579 activity following nutrient and oxygen deprivation is not merely a consequence of
580 changing metabolic conditions but instead is an essential adaptation.
581

582 **Arid conditions create a selective and non-redundant dependency on Bcl-xL**

583 Inhibitors of the TCA cycle and OXPHOS, including the TCA cycle inhibitor CPI-
584 613, have demonstrated efficacy in PDAC pre-clinical models (47–49) but limited
585 success in PDAC clinical trials (https://www.healio.com/news/hematology-
586 oncology/20211028/devimistat-regimen-fails-to-extend-os-in-metastatic-pancreatic-
587 cancer) (50). Therefore, we re-examined our CRISPR data to identify other tractable
588 vulnerabilities specific to metabolically deprived slow-cycling cells. Among genes
589 exclusively depleted under both early and late arid conditions, but not under fertile
590 conditions, the BCL-2 family member *Bcl2l1*, encoding Bcl-xL, stood out as one of the
591 most strongly selected genes (Fig. 3A) and its expression increased under arid
592 conditions (Fig. 3B). Bcl-xL is best known for its ability to inhibit apoptosis (51,52), but it
593 also regulates mitochondrial function (52) and cell cycle progression (53,54). Given that
594 these three cellular activities are features of the metabolic adaptation in our
595 experimental system, we hypothesized that arid conditions create a selective
596 dependency on Bcl-xL that is not shared by pancreatic cancer cells under fertile
597 conditions. No other canonical BCL2-family members were enriched or depleted under
598 either fertile or arid conditions (Fig. 3A), suggesting that Bcl-xL may have a unique
599 function in slow-cycling metabolically deprived cancer cells.

600 We first confirmed the dependency for Bcl-xL by knocking out the *BCL2L1* gene
601 with two independent sgRNAs (Fig. S6A). In line with our CRISPR screen results, Bcl-
602 xL-deficient cells exhibited reduced fitness in a competition assay under arid but not
603 fertile conditions (Fig. 3C) and were eliminated even if cells were already adapted to
604 arid conditions (Fig. S6B). This requirement for Bcl-xL was validated in 2 additional

human PDAC cell lines (AsPC-1 and HPAC), a murine PDAC cell line (MH6620c1), and 5 other non-PDAC cancer cell lines (Fig. 3D and Fig. S6C,D). Interestingly, BxPC3 cells, which lack a KRAS mutation, did not show differential dependence. Cell viability was high and comparable between empty vector (EV) and Bcl-xL-deficient cells under fertile conditions (Fig. S6E). By contrast, Bcl-xL-deficient cells exhibited decreased viability within 1 day of culture under arid conditions (Fig. 3E). Therefore, Bcl-xL protects pancreatic cancer cells from cell death following nutrient and oxygen deprivation but is dispensable under nutrient replete conditions.

To further confirm this Bcl-xL dependency, we employed a potent and highly selective Bcl-xL inhibitor, A-1155463, which is based on the 2-(fluorophenoxy)propyl)thiazole-4-carboxylic acid structure (55). Exposure of either PANC-1, MH6620c1, AsPC-1, or HPAC cells to A-1155463 *in vitro* resulted in a significant dose-dependent loss of viability under arid conditions, whereas the drug had no effect on cells under fertile conditions, even at doses over 10 μM (Fig. 3F and Fig. S6F-H). A1155463-mediated cell death was inhibited by the pan-caspase inhibitor Z-VAD-FMK (Fig. S6I), indicating that apoptotic cell death contributed at least partially to the reduced fitness of Bcl-xL-deficient cells grown under arid conditions.

Because the arid medium composition was determined empirically, we sought to determine whether the dependency on Bcl-xL extended to physiologically-defined metabolic conditions. To this end, we exploited tumor interstitial fluid medium (TIFM) – media defined by direct measurement of metabolite concentrations in the interstitial space of murine pancreatic tumors (36). Consistent with our results using arid medium, PANC1 cells grown in TIFM medium (1% O_2) were also dependent on Bcl-xL for

628 survival (Fig. S7A-B). Moreover, cells grown in arid or TIFM medium showed similar
629 sensitivity to the Bcl-xL inhibitor A-1155463 (Fig. S7C). Hence, Bcl-xL function is
630 required for cell survival under diverse conditions of metabolic deprivation.

631 Bcl-xL exerts protective effects under a variety of stress conditions (52). To
632 determine what triggers Bcl-xL dependency under arid conditions, we conducted "add-
633 back" experiments in which we re-introduced various nutrients – either alone or in
634 combination and under hypoxic or normoxic conditions – and then assessed the
635 proportions of two Bcl-xL-deficient tumor cell clones in competition with empty vector
636 (EV) cells. No single nutrient, or normoxia, was able to rescue either Bcl-xL-deficient
637 clone under hypoxic conditions (Fig. 3G and Fig. S7D). Paradoxically, re-introducing
638 10% FBS exacerbated depletion of Bcl-xL-deficient cells, while co-addition of FBS and
639 glucose together rescued the phenotype (Fig. 3G), suggesting that Bcl-xL may be
640 particularly important under conditions where 'biosynthetic pressure' is high, but carbon
641 fuel is low (see Fig. S1C). Taken together, these results suggest that metabolic
642 deprivation creates a selective and non-redundant dependency on Bcl-xL.

643

644 **Bcl-xL promotes the survival of cancer cells in poorly perfused tumor regions**

645 To test whether Bcl-xL is essential for pancreatic cancer cells *in vivo*, we
646 inoculated empty vector (GFP+) or Bcl-xL-deficient (mCherry+) PANC-1 cells into the
647 flanks of NOD.SCID mice. Consistent with their reduced viability under arid conditions *in*
648 *vitro* (Fig. 3E), Bcl-xL-deficient cells gave rise to a decreased tumor burden (Fig. 4A-B
649 and Fig. S8) that was associated with a 4-5-fold increase in apoptosis (Fig. 4C). Next,
650 we performed a competition experiment in which we subcutaneously implanted control

651 EV-GFP and Bcl-xL-deficient-mCherry tumor cells at a 1:1 ratio, injected TMR-dextran
652 (IV) prior to sacrifice, and examined the resulting tumors. In line with our *in vitro* results,
653 Bcl-xL-deficient tumor cells were consistently depleted but not eradicated in the mixed
654 tumors (Fig. 4D-E). Analysis of spatial distributions revealed that Bcl-xL-deficient cells
655 were less abundant as the distance from perfused blood vessels increased (Fig. 4F),
656 indicating a selective requirement for Bcl-xL in poorly perfused regions.

657 Next, we sought to determine whether A-1155463 results in a similar perfusion-
658 dependent cell lethality *in vivo*. PANC-1-GFP xenografts were allowed to grow to 6-9
659 mm and then treated with an intratumoral injection of A-1155463 or vehicle for 24 hours,
660 followed by an injection of TMR-dextran prior to sacrifice. Tumors were then sectioned
661 and stained with antibodies against CC3 to quantify apoptosis as a function of distance
662 from perfused blood vessels. GFP+ tumor cells within 200 μm of perfused blood vessels
663 exhibited similar rates of CC3+ staining between A-1155463 and vehicle-treated groups
664 (Fig. 4G). By contrast, GFP+ tumor cells >400 μm from perfused blood vessels
665 exhibited a 2-4-fold increase in CC3+ staining in the A-1155463 treatment group (Fig.
666 4G), indicating that sensitivity to Bcl-xL inhibition is positively correlated with distance
667 from perfused blood vessels. We then treated a separate cohort of mice with a
668 combination of Gemcitabine and Nab-paclitaxel (Gem/nP), which is standard-of-care
669 chemotherapy for PDAC (56), or vehicle control. In contrast to our findings with A-
670 1155463, sensitivity to Gem/nP was limited to GFP+ cells located within 200 μm of
671 perfused blood vessels (Fig. 4H). These results complement our *in vitro* studies and
672 suggest that cancer cells residing in well perfused tumor compartments are more

673 sensitive to cytotoxic chemotherapy while cancer cells residing in poorly perfused tumor
674 compartments are more sensitive to Bcl-xL inhibition.

675 These findings raised the possibility that simultaneous targeting of proliferating
676 and slow-cycling tumor cells might provide a more potent anti-tumor effect than either
677 therapy alone. To this end, we established subcutaneous tumors (6-9 mm in diameter)
678 using the murine PDAC clone MH6620c1 and treated tumor-bearing mice with either (i)
679 vehicle, (ii) A-1331852 (an orally available form of A-1155463 (57)), (iii) Gem/nP, or (iv)
680 the combination of A-1331852 and Gem/nP (Fig. 4I). While either regimen alone had
681 modest effects on tumor volume, the combination of A-1331852 and Gem/nP led to a
682 clear inhibition of tumor growth, including several tumor regressions (Fig. 4I). These
683 results provide proof-of-concept that an approach which targets both the rapid- and
684 slow-cycling compartments of a tumor may provide synergistic therapeutic benefit.

685

686 **Bcl-xL expression is restricted to slow-cycling cancer cells in human PDAC**

687 We next examined the expression of Bcl-xL (*BCL2L1*) in human PDAC. An
688 analysis of the TCGA dataset revealed *BCL2L1* to be expressed in pancreatic tumors
689 (PAAD) at a higher level compared to most other tumor types (Fig. 5A). *BCL2L1*
690 transcripts were significantly more abundant in tumors compared to adjacent normal
691 pancreatic tissue (Fig. 5B), consistent with the hypovascular and hypoxic nature of most
692 pancreatic tumors (28,58). Moreover, *BCL2L1* expression was highly correlated with the
693 overall survival of PDAC patients compared to patients with other types of cancer (Fig.
694 5C-D), a prognostic correlation shared by its closest relative (*BCL2L2*) but no other
695 BCL-2 family members (Fig. S9A).

To determine whether the expression of *BCL2L1* is linked to slow-cycling state in human cancer, we analyzed three published single cell RNA-seq (scRNA-seq) datasets (59–61) and annotated cancer cells as either proliferating or quiescent (Fig. 5E). In agreement with previous observations (32), only a minority of cancer cells exhibited a proliferative gene signature, while most cancer cells exhibited a slow-cycling gene signature characterized by the expression of *CDKN2A* and *CDKN2B* (Fig. 5E and Fig. S9B). Consistent with our predictions, expression of *BCL2L1* was markedly higher in the slow-cycling population compared to the proliferating population (Fig. 5E).

Next, we examined the functional annotations of genes that were differentially expressed between rapidly and slowly cycling cancer cells in human PDAC. This revealed that the gene programs which distinguished these two populations in human PDAC tumors bore a striking similarity to those that were up-regulated or down-regulated in PANC-1 grown in fertile vs. arid conditions *in vitro* (Fig. 5F and Fig. S9C). Most notably, hypoxia, NFkB and cell cycle inhibitory pathways were enriched in slow-cycling cells from both human tumors and arid-cultured cells, while oxidative phosphorylation and targets of E2F and MYC were enriched in rapidly cycling cancer cells from both human tumors and fertile-cultured cells (Fig. 5F and Fig. S9C). Taken together, these results suggest that the genes and pathways found to be dysregulated in our *in vitro* experimental system – including Bcl-xL (BCL2L1) – recapitulate the gene expression features that distinguish the rapidly and slowly cycling compartments of human PDAC tumors.

Bcl-xL protects cells from “inappropriate” biosynthesis

We next investigated the mechanism by which Bcl-xL promotes cell survival under arid conditions. We first performed RNA sequencing of Bcl-xL-deficient and EV-GFP cells grown under arid conditions. Pathways involved in cell cycle regulation, including targets of MYC and E2F, were the most highly enriched programs in Bcl-xL KO cells (Fig. 6A and Fig. S10A). Immunoblotting and immunostaining of PDAC cells (PANC-1, AsPC-1, HPAC, and BxPC-3) revealed that control cells downregulate MYC protein levels, as well as S6 phosphorylation, under arid conditions, an effect that was blunted in the absence of Bcl-xL (Fig. 6B and Fig. S10B,C). These results suggest that Bcl-xL constrains the biosynthetic and pro-proliferative activities that normally accompany metabolic deprivation.

Bcl-xL has been shown to act as a tumor suppressor by restricting the proliferation of cancer cells in certain contexts (53,54,62). In line with these anti-proliferative properties, Bcl-xL-deficient cells exhibited a 3-4-fold increase in EdU incorporation under arid conditions (Fig. 6C), resulting in over 50% of cancer cells staining positively for Ki-67 (Fig. 6D). By contrast, Bcl-xL-deficiency had no effect on EdU incorporation or Ki-67 positivity under fertile conditions, where proliferation rates were already high (Fig. S10D-E). Similar results were obtained following Bcl-xL ablation in additional pancreatic cancer cell lines under arid conditions (Fig. S10F). Given that Bcl-xL deficient cells exhibit increased rates of cell death when cultured under arid conditions (Fig. 3C), these results are consistent with Bcl-xL acting to suppress a “lethal proliferation.” Bcl-xL-deficient cells co-cultured with control (EV-GFP) cells similarly exhibited increased Ki-67 staining (Fig. S10G), indicating that Bcl-xL’s proliferation-constraining activity is cell autonomous.

742 To better understand the relationship between cell cycle progression and cell
743 death in Bcl-xL-deficient cells, we used a PCNA-interacting protein-fluorescent
744 ubiquitination-based cell cycle indicator (PIP-FUCCI) reporter, which accurately reports
745 cells in different phases of the cell cycle (21) (Fig. 6E). Using time-lapse fluorescent
746 microscopy, we followed the fate of over 800 control (EV) cells or Bcl-xL-deficient cells
747 by direct visualization under either fertile or arid conditions. Using this fate-mapping
748 approach, we observed a ~3-4-fold increase in G1/S transitions in Bcl-xL-deficient cells
749 compared to control cells (Fig. 6F) but no significant differences in transitions through
750 other phases of the cell cycle (Fig. S10H, and Movies S1-S2) or mitosis (Fig. 6G). As
751 expected, the fraction of cells transitioning from G1 phase to S phase (comparing EV
752 and Bcl-xL-deficient cells) did not increase under fertile conditions (Fig. S10I and
753 Movies S3-4). This suggests that the increased S phase entry caused by Bcl-xL loss
754 does not translate into an increase in cellular progeny.

755 We next examined our time-lapse microscopy data to determine whether certain
756 phases of the cell cycle were associated with increased cell death in the absence of Bcl-
757 xL. Under arid conditions, control (EV) cells exhibited low rates of cell death in the G1
758 (2%) and S (0%) phases of the cell cycle, while 8% of control cells died during the G2/M
759 phase (Fig. 6H). By contrast, Bcl-xL-deficiency was associated with increased cell death
760 at all stages of the cell cycle, particularly during S phase (20%) and G2/M (19%) (Fig.
761 6H). To determine whether the cell death induced by Bcl-xL knockout was related to this
762 increase in proliferation, we treated cells with the CDK4/6 inhibitor abemaciclib, a potent
763 cell cycle inhibitor (Fig. S10J, Movie S5). Abemaciclib treatment rescued cell viability in

764 all stages of the cell cycle (Fig. 6H), suggesting that cell cycle transit is responsible for
765 the increased lethality caused by Bcl-xL loss under arid conditions (53,62).

766 Finally, we examined whether Bcl-xL deficiency has similar effects on cell
767 proliferation in PDAC tumors *in vivo*. Tumors derived from control (EV) and Bcl-xL-
768 deficient cancer cells were stained for Ki-67 as a function of distance from a TMR-
769 dextran perfused blood vessel. Control tumors exhibited a typical gradient of Ki-67
770 staining (higher near blood vessels and lower further away) (Fig. 6I, left). In contrast, Ki-
771 67+ cells were distributed throughout the axis of perfusion in Bcl-xL-deficient tumors
772 (Fig. 6I, right, and Fig. S10K), giving further support to the notion that Bcl-xL represses
773 proliferation in nutrient deprived regions of tumors.

774

775 **Biosynthetic pressure is lethal to metabolically deprived PDAC cells**

776 The results from our CRISPR screen and metabolic “add-back” experiments
777 suggested that biosynthesis and/or proliferation are lethal to metabolically deprived
778 cells, which may lack sufficient resources to meet the demands of cell division. To
779 further explore this hypothesis, we extended our add-back studies, focusing on the
780 addition of serum, which reduced fitness, and glucose, which increased fitness (Fig.
781 3G). Consistent with our previous findings, addition of 10% FBS to cells grown under
782 arid conditions prompted an increase in the fraction of EdU+ cells (Fig. 7A) and a
783 concomitant increase in cell death that could be rescued with glucose (Fig. 7B). These
784 results suggest that auxiliary fuel sources can overcome the lethal proliferation
785 associated with extreme metabolic deprivation.

786 To directly determine whether biosynthetic activity is responsible for cell lethality
787 under arid conditions, we exposed control- and serum-treated cancer cells to several
788 small molecule inhibitors of biosynthesis, including a CDK4/6 inhibitor (Abemaciclib),
789 mTOR inhibitors (Rapamycin and Torin1), and a protein synthesis inhibitor
790 (Cycloheximide). We observed that these inhibitors reduced both proliferation (Fig. 7C)
791 and cell death (Fig. 7D). Together, these results suggest that biosynthesis and
792 proliferation in the absence of adequate resources reduces the viability of metabolically
793 deprived cancer cells.
794

Discussion

Metabolic vulnerabilities of hypoxic, nutrient-deprived pancreatic cancer cells

It is well-established that the tumor microenvironment differs proximal and distal to blood vessels, with hypoxia being increased distally and associated with poorly perfused, slowly cycling cells. While studies of interstitial tumor fluid metabolites and other media formulations approximating physiological conditions have been instructive (36,63,64), these studies are unable to resolve differences between well perfused versus hypoxic, poorly perfused tumor regions. It is increasingly recognized that standard cell culture conditions, which have been optimized to promote cell proliferation at 20% oxygen, differ considerably from the hypoxic and nutrient deprived tumor microenvironments that dominate most solid tumors *in vivo* (10). Previous investigations have deprived cancer cells of single or pairs of nutrients (13,14,16,65,66) conditions that are unlikely to mimic nutrient availability in poorly-perfused tumor regions. Central to our efforts to recapitulate the poorly perfused, hypoxic microenvironment, we have identified a cell culture system that deprives cancer cells of multiple nutrients, resulting in slow cycling cells. The findings with our cell culture system were corroborated by studies using tumor interstitial fluid medium (TIFM) (36).

The “arid condition” used in this study was able to induce and maintain a stable and persistent slow-cycling state by depriving cells of the full spectrum of metabolites and oxygen, mimicking the poorly perfused tumor microenvironment. Using this experimental system, we found that two broadly-delineated cellular states in solid tumors – a rapidly cycling state characterized by metabolic sufficiency and a slow-

818 cycling, scavenger-like state driven by nutrient and oxygen deprivation – manifest
819 markedly different dependencies. Rapidly cycling cells are sensitive to Gemcitabine, as
820 expected, while slow-cycling cells are chemoresistant. As such, uncovering the
821 metabolic vulnerabilities of these slow-cycling cells using an unbiased gRNA
822 CRISPR/Cas 9 screening would be foundational for novel therapeutic strategies.

823 Cancer cells cultured in the arid condition experienced extensive transcriptional
824 rewiring, conferring resistance to treatments targeting biosynthesis or proliferation and,
825 at the same time, generating dependencies on pathways that are not as important in
826 rapidly cycling, glycolytic cells. Intriguingly, we found that slow-cycling cancer cells
827 following nutrient and oxygen deprivation exhibited an unforeseen dependency on
828 OXPHOS, surprising given prior evidence suggesting that cancer cells can have a
829 reduced dependency on OXPHOS in low-glucose conditions (13) or hypoxia (16,65).
830 These observations highlight the value of an experimental system in which multiple
831 nutrients are withdrawn simultaneously. Importantly, the pre-clinical success of agents
832 that target OXPHOS might reflect the increased sensitivity of tumors, like PDAC, that
833 are metabolically deprived *in vivo* (47–49,67).

834 Adaptation to nutrient-deprived conditions engages various mechanisms for
835 acquiring or repurposing metabolic resources to support survival, including autophagy,
836 macropinocytosis, and anaplerosis (68). Meanwhile, cells reduce energy expenditure to
837 avoid exhaustion (46,69) or loss of homeostasis (70,71). Consistent with this
838 hypothesis, we found that promoting biosynthesis and proliferation under metabolically
839 deprived conditions, by depletion of cell growth inhibitors, such as loss of TSC2, or
840 repletion of serum, resulted in loss of fitness and cell death. Taken together, these

observations reinforce the conclusion that reactivating cell growth programs hinders the survival of slow-cycling cells in nutrient deprived, hypoxic microenvironments.

Bcl-xL promotes the survival of slow-cycling tumor cells following nutrient deprivation

The observation that gRNAs directed at Bcl-xL were among the top ones selectively depleted in arid conditions was not unexpected given its role as an inhibitor of apoptosis (52). However, Bcl-xL was not redundant with other Bcl-2 family members following nutrient deprivation (72–74). Notably, Bcl-xL suppresses cell cycle progression, a property that correlates with its pro-survival effects (53). Efforts to decouple the cell cycle and survival function have yielded conflicting results (53,75,76). In this study, we found that depletion of Bcl-xL promotes both cell cycle progression and cell death within the same cancer cell population under arid conditions. Furthermore, pharmacological inhibition of CDK4/6, mTOR, or protein synthesis relieved the dependency on Bcl-xL under arid conditions. This suggests that at least under our arid conditions, Bcl-xL is causally related to its quiescent function under nutrient deprived conditions.

While Bcl-xL has been extensively studied *in vitro,* less is known about its function *in vivo* and it is mainly studied for its anti-apoptotic function (77). Here, we provide evidence that Bcl-xL functions in poorly perfused regions and maintains tumor cell quiescence that may be essential for preserving this chemoresistant population. Concordantly, Bcl-xL KO PDAC tumors grow slower, despite the increased drive for biosynthesis (phospo-S6) and proliferation (Ki67/EdU), a result that is in agreement with the paradoxical response observed in PDAC tumors treated with rapamycin (68). The

finding that Bcl-xL expression is enriched in slow-cycling cancer cells in human PDAC suggests that the relationships between metabolic microenvironments and survival programs reported here are conserved in human tumors.

The Bcl-2 family of apoptosis inhibitors has been the focus of considerable attention over the years as potential targets for cancer therapy, but the majority of pre-clinical studies and clinical trials testing Bcl-2 family inhibitors as monotherapy have shown limited efficacy in solid tumors (78). Consistent with these findings, pharmacological inhibition of Bcl-xL with the inhibitor A-1331852 had only a modest effect on tumor growth *in vivo*. In contrast, we found that this drug markedly enhanced the activity of standard-of-care Gemcitabine/Nab-paclitaxel, a synergy likely due to complementary effects on chemoresistant cells in poorly perfused tumor regions and chemo-sensitive cells in well perfused tumor regions although we cannot exclude enhancements of gemcitabine killing in well-perfused regions due to loss of control of apoptosis as an additional factor. These observations establish the potential of combining treatments that target both the rapidly and slowly cycling subsets of cancer cells, as treatments eliminating either subset alone are insufficient (2).

881 **Acknowledgements**

882 We are grateful to A. Rustgi, F. Zhang, D. Feldser, C. Vakoc, J. Shi, A. Minn, and J.
883 Debnath for providing reagents, C. Simon, K. Wellen, C. Halbrook, Z. Stein and M. Noji
884 for helpful advice and comments on the manuscript, and members of the Stanger and
885 Dang laboratories for critical input and encouragement. This work was supported by
886 grants from NIH (CA229803, CA252225, P30ES013508), the Abramson Family Cancer
887 Research Institute, the Abramson Cancer Center, and the NIH/Penn Center for
888 Molecular Studies in Digestive and Liver Diseases (P30DK050306). Generation of the
889 TIFM model was supported by the Ludwig Center for Metastasis Research at University
890 of Chicago, the Pancreatic Cancer Action Network, the Brinson Foundation, the
891 National Pancreas Foundation, the Cancer Research Foundation and University of
892 Chicago's Comprehensive Cancer Center's NCI Cancer Center
893 Support Grant (P30CA014599). J.L. is the recipient of a graduate student training
894 fellowship from the Blavatnik Family Foundation.

895

References

1. Sahin AA, Ro JY, El-Naggar AK, Wilson PL, Teague K, Blick M, et al. Tumor proliferative fraction in solid malignant neoplasms: A comparative study of Ki-67 immunostaining and flow cytometric determinations. Am J Clin Pathol. 1991;96:512–9.
2. Yano S, Zhang Y, Miwa S, Tome Y, Hiroshima Y, Uehara F, et al. Spatial-temporal FUCCI imaging of each cell in a tumor demonstrates locational dependence of cell cycle dynamics and chemoresponsiveness. Cell Cycle 2014;13:2110–9.
3. Granada AE, Jiménez A, Stewart-Ornstein J, Blüthgena N, Reber S, Jambhekar A, et al. The effects of proliferation status and cell cycle phase on the responses of single cells to chemotherapy. Mol Biol Cell. 2020;31:845–57.
4. Rossari F, Zucchinetti C, Buda G, Orciuolo E. Tumor dormancy as an alternative step in the development of chemoresistance and metastasis - clinical implications. Cell Oncol. Cellular Oncology 2020;43:155–76.
5. Pinto B, Henriques AC, Silva PMA, Bousbaa H. Three-dimensional spheroids as in vitro preclinical models for cancer research. Pharmaceutics. 2020;12:1–38.
6. Porschen R, Classen S, Piontek M, Borchard F. Vascularization of Carcinomas of the Esophagus and Its Correlation with Tumor Proliferation. Cancer Res. 1994;54:587–91.
7. Bartlett R, Everett W, Lim S, Natasha G, Loizidou M, Jell G, et al. Personalized in vitro cancer modeling — Fantasy or reality? Transl Oncol [Internet]. Neoplasia Press, Inc. 2014;7:657–64.

8. Kumar S, Sharife H, Kreisel T, Mogilevsky M, Bar-Lev L, Grunewald M, et al. Intra-Tumoral Metabolic Zonation and Resultant Phenotypic Diversification Are Dictated by Blood Vessel Proximity. Cell Metab. 2019;30:201-211.
9. Kyle AH, Baker JHE, Minchinton AI. Targeting quiescent tumor cells via oxygen and IGF-I supplementation. Cancer Res. 2012;72:801–9.
10. Mayers JR, Vander Heiden MG. Famine versus feast: Understanding the metabolism of tumors in vivo. Trends Biochem Sci. 2015;40:130–40.
11. Nik Nabil WN, Xi Z, Song Z, Jin L, Zhang XD, Zhou H, et al. Towards a Framework for Better Understanding of Quiescent Cancer Cells. Cells 2021;10:562.
12. Jain IH, Calvo SE, Markhard AL, Skinner OS, To TL, Ast T, et al. Genetic Screen for Cell Fitness in High or Low Oxygen Highlights Mitochondrial and Lipid Metabolism. Cell 2020;181:716-727.
13. Birsoy K, Possemato R, Lorbeer FK, Bayraktar EC, Thiru P, Yucel B, et al. Metabolic determinants of cancer cell sensitivity to glucose limitation and biguanides. Nature 2014;508:108–12.
14. Keenan MM, Liu B, Tang X, Wu J, Cyr D, Stevens RD, et al. ACLY and ACC1 Regulate Hypoxia-Induced Apoptosis by Modulating ETV4 via α-ketoglutarate. PLoS Genet. 2015;11:1–29.
15. Yoshino S, Hara T, Weng JS, Takahashi Y, Seiki M, Sakamoto T. Genetic screening of new genes responsible for cellular adaptation to hypoxia using a genome-wide shRNA library. PLoS One. 2012;7:e35590.
16. Thomas LW, Esposito C, Morgan RE, Price S, Young J, Williams SP, et al.

Genome-wide CRISPR/Cas9 deletion screen defines mitochondrial gene essentiality and identifies routes for tumour cell viability in hypoxia. Commun Biol. 2021;4:1–12.

17. Li J, Byrne KT, Yan F, Yamazoe T, Chen Z, Baslan T, et al. Tumor Cell-Intrinsic Factors Underlie Heterogeneity of Immune Cell Infiltration and Response to Immunotherapy. Immunity. 2018;49:178-193.

18. Doench JG, Root D. Optimized sgRNA design to maximize activity and minimize off-target effects of CRISPR-Cas9 Synthesis of an arrayed sgRNA library targeting the human genome. Nat Biotechnol. 2016;34:184–91.

19. Shalem O, Sanjana NE, Hartenian E, Shi X, Scott DA, Heckl D, et al. Shalem et al., 2014. Science (80-). 2014;343:84–7.

20. Guo L, Worth AJ, Mesaros C, Snyder NW, Jerry D, Blair IA. Diisopropylethylamine/hexafluoroisopropanol-mediated ion- pairing UHPLC-MS for phosphate and carboxylate metabolite analysis: utility for studying cellular metabolism. Rapid Commun Mass Spectrom. 2016;30:1835–45.

21. Grant GD, Kedziora KM, Limas JC, Cook JG, Purvis JE. Accurate delineation of cell cycle phase transitions in living cells with PIP-FUCCI. Cell Cycle 2018;17:2496–516.

22. Tarumoto Y, Lu B, Somerville TDD, Huang YH, Milazzo JP, Wu XS, et al. LKB1, Salt-Inducible Kinases, and MEF2C Are Linked Dependencies in Acute Myeloid Leukemia. Mol Cell 2018;69:1017-1027.

23. Walter DM, Venancio OS, Buza EL, Tobias JW, Deshpande C, Gudiel A, et al. Systematic in vivo inactivation of chromatin- regulating enzymes identifies Setd2

as a potent tumor suppressor in lung adenocarcinoma. Cancer Res. 2017;77:1719–29.

24. Shi J, Wang E, Milazzo JP, Wang Z, Kinney JB, Vakoc CR. 2015.14. Nat Biotechnol. 2015;33:661–7.

25. N'Diaye EN, Kajihara KK, Hsieh I, Morisaki H, Debnath J, Brown EJ. PLIC proteins or ubiquilins regulate autophagy-dependent cell survival during nutrient starvation. EMBO Rep. 2009;10:173–9.

26. Love MI, Huber W, Anders S. Moderated estimation of fold change and dispersion for RNA-seq data with DESeq2. Genome Biol. 2014;15:1–21.

27. Győrffy B. Survival analysis across the entire transcriptome identifies biomarkers with the highest prognostic power in breast cancer. Comput Struct Biotechnol J. 2021;19:4101–9.

28. Olive KP, Jacobetz MA, Davidson CJ, Gopinathan A, McIntyre D, Honess D, et al. Inhibition of Hedgehog signaling enhances delivery of chemotherapy in a mouse model of pancreatic cancer. Science (80-). 2009;324:1457–61.

29. Koong AC, Mehta VK, Le QT, Fisher GA, Terris DJ, Brown JM, et al. Pancreatic tumors show high levels of hypoxia. Int J Radiat Oncol Biol Phys. 2000;48:919–22.

30. Kamphorst JJ, Nofal M, Commisso C, Hackett SR, Lu W, Grabocka E, et al. Human pancreatic cancer tumors are nutrient poor and tumor cells actively scavenge extracellular protein. Cancer Res. 2015;75:544–53.

31. Lee KE, Spata M, Bayne LJ, Buza EL, Durham AC, Allman D, et al. Hif1a deletion reveals pro-neoplastic function of B cells in pancreatic neoplasia. Cancer Discov.

2016;6:256–69.

32. Aiello NM, Bajor DL, Norgard RJ, Sahmoud A, Bhagwat N, Pham MN, et al. Metastatic progression is associated with dynamic changes in the local microenvironment. Nat Commun. 2016;7:12819.

33. Aeffner F, Martin NT, Peljto M, Black JC, Major JK, Jangani M, et al. Quantitative assessment of pancreatic cancer precursor lesions in IHC-stained tissue with a tissue image analysis platform. Lab Investig. 2016;96:1327–36.

34. Ströbel P, Ellenrieder V, Maisonneuve P, Neesse A. Stromal Features of the Primary Tumor Are Not Pancreatic Cancer. Cells 2019;9:1–13.

35. Ferrara C, Tessari G, Poletti A, Giacon C, Meggiato T, Martines D, et al. Ki-67 and c-jun expression in pancreatic cancer: a prognostic marker? Oncol Rep 1999;6:1117–39.

36. Sullivan MR, Danai L V., Lewis CA, Chan SH, Gui DY, Kunchok T, et al. Quantification of microenvironmental metabolites in murine cancers reveals determinants of tumor nutrient availability. Elife. 2019;8:1–27.

37. Zaidi M, Fu F, Cojocari D, McKee TD, Wouters BG. Quantitative Visualization of Hypoxia and Proliferation Gradients Within Histological Tissue Sections. Front Bioeng Biotechnol. 2019;7:1–9.

38. Commisso C, Davidson SM, Soydaner-Azeloglu RG, Parker SJ, Kamphorst JJ, Hackett S, et al. Macropinocytosis of protein is an amino acid supply route in Ras-transformed cells. Nature. 2013;497:633–7.

39. Yang A, Herter-Sprie G, Zhang H, Lin EY, Biancur D, Wang X, et al. Autophagy sustains pancreatic cancer growth through both cell-autonomous and

1011 nonautonomous mechanisms. Cancer Discov. 2018;8:276-87.
1012 40. Gameiro PA, Struhl K. Nutrient Deprivation Elicits a Transcriptional and
1013 Translational Inflammatory Response Coupled to Decreased Protein Synthesis.
1014 Cell Rep. 2018;24:1415–24.
1015 41. Awasthi N, Zhang C, Schwarz AM, Hinz S, Wang C, Williams NS, et al.
1016 Comparative benefits of nab-paclitaxel over gemcitabine or polysorbate-based
1017 docetaxel in experimental pancreatic cancer. Carcinogenesis. 2013;34:2361–9.
1018 42. Huggett MT, Tudzarova S, Proctor I, Loddo M, Keane MG, Stoeber K, et al. Cdc7
1019 is a potent anti-cancer target in pancreatic cancer due to abrogation of the DNA
1020 origin activation checkpoint. Oncotarget. 2016;7:18495–507.
1021 43. Cencic R, Carrier M, Galicia-Vázquez G, Bordeleau ME, Sukarieh R, Bourdeau A,
1022 et al. Antitumor activity and mechanism of action of the cyclopenta[b]benzofuran,
1023 silvestrol. PLoS One. 2009;4:e5223.
1024 44. Zachar Z, Marecek J, Maturo C, Gupta S, Stuart SD, Howell K, et al. Non-redox-
1025 active lipoate derivates disrupt cancer cell mitochondrial metabolism and are
1026 potent anticancer agents in vivo. J Mol Med. 2011;89:1137–48.
1027 45. Zhong Y, Li X, Yu D, Li X, Li Y, Long Y, et al. Application of mitochondrial
1028 pyruvate carrier blocker UK5099 creates metabolic reprogram and greater stem-
1029 like properties in LnCap prostate cancer cells in vitro. Oncotarget 2015;6:37758–
1030 69.
1031 46. Liu L, Cash TP, Jones RG, Keith B, Thompson CB, Simon MC. Hypoxia-induced
1032 energy stress regulates mRNA translation and cell growth. Mol Cell.
1033 2006;21:521–31.

47. Rajeshkumar N V, Yabuuchi S, Pai SG, Oliveira E De, Hidalgo M, Maitra A, et al. Treatment of Pancreatic Cancer Patient – Derived Xenograft Panel with Metabolic Inhibitors Reveals Ef fi cacy of Phenformin. Clin Cancer Res. 2017;23:5639–48.
48. Masoud R, Reyes-Castellanos G, Lac S, Garcia J, Dou S, Shintu L, et al. Targeting Mitochondrial Complex I Overcomes Chemoresistance in High OXPHOS Pancreatic Cancer. Cell Reports Med. 2020;1:100143.
49. Lee KC, Maturo C, Perera CN, Luddy J, Rodriguez R, Shorr R. Translational assessment of mitochondrial dysfunction of pancreatic cancer from in vitro gene microarray and animal efficacy studies, to early clinical studies, via the novel tumor-specific anti-mitochondrial agent, CPI-613. Ann Transl Med. 2014;2:1–10.
50. Philip PA, Buyse ME, Alistar AT, Lima CM, Luther S, Pardee TS, et al. A phase III open-label trial to evaluate efficacy and safety of CPI-613 plus modified FOLFIRINOX (mFFX) versus FOLFIRINOX (FFX) in patients with metastatic adenocarcinoma of the pancreas. Futur Oncol. 2019;15:3189–96.
51. Boise LH, González-García M, Postema CE, Ding L, Lindsten T, Turka LA, et al. Bcl-X, a Bcl-2-Related Gene That Functions As a Dominant Regulator of Apoptotic Cell Death. Cell 1993;74:597–608.
52. Michels J, Kepp O, Senovilla L, Lissa D, Castedo M, Kroemer G, et al. Functions of BCL-XL at the interface between cell death and metabolism. Int J Cell Biol. 2013;2013:705294.
53. Janumyan YM, Sansam CG, Chattopadhyay A, Cheng N, Soucie EL, Penn LZ, et al. Bcl-xL/Bcl-2 coordinately regulates apoptosis, cell cycle arrest and cell cycle entry. EMBO J. 2003;22:5459–70.

54. Janumyan Y, Cui Q, Yan L, Sansam CG, Valentin M, Yang E. G0 function of BCL2 and BCL-xL requires BAX, BAK, and p27 phosphorylation by mirk, revealing a novel role of BAX and BAK in quiescence regulation. J Biol Chem. 2008;283:34108–20.

55. Tao ZF, Hasvold L, Wang L, Wang X, Petros AM, Park CH, et al. Discovery of a potent and selective BCL-XLinhibitor with in vivo activity. ACS Med Chem Lett. 2014;5:1088–93.

56. Ducreux M, Seufferlein T, Van Laethem JL, Laurent-Puig P, Smolenschi C, Malka D, et al. Systemic treatment of pancreatic cancer revisited. Semin Oncol. 2019;46:28–38.

57. Leverson JD, Phillips DC, Mitten MJ, Boghaert ER, Diaz D, Tahir SK, et al. Exploiting selective BCL-2 family inhibitors to dissect cell survival dependencies and define improved strategies for cancer therapy. Sci Transl Med. 2015;7:1–12.

58. Kahn BM, Lucas A, Alur RG, Wengyn MD, Schwartz GW, Li J, et al. The vascular landscape of human cancer. J Clin Invest. 2021;131:1–16.

59. Peng J, Sun BF, Chen CY, Zhou JY, Chen YS, Chen H, et al. Single-cell RNA-seq highlights intra-tumoral heterogeneity and malignant progression in pancreatic ductal adenocarcinoma. Cell Res. 2019;29:725–38.

60. Steele NG, Carpenter ES, Kemp SB, Sirihorachai V, The S, Delrosario L, et al. HHS Public Access. Nat cancer. 2021;1:1097–112.

61. Lin W, Noel P, Borazanci EH, Lee J, Amini A, Han IW, et al. Single-cell transcriptome analysis of tumor and stromal compartments of pancreatic ductal adenocarcinoma primary tumors and metastatic lesions. Genome Med.

2020;12:80.

62. Linette GP, Li Y, Roth K, Korsmeyer SJ. Cross talk between cell death and cell cycle progression: BCL-2 regulates NFAT-mediated activation. Proc Natl Acad Sci U S A. 1996;93:9545–52.

63. Rossiter NJ, Huggler KS, Adelmann CH, Keys HR, Soens RW, Sabatini DM, et al. CRISPR screens in physiologic medium reveal conditionally essential genes in human cells. Cell Metab. 2021;33:1248-1263.

64. Voorde J Vande, Ackermann T, Pfetzer N, Sumpton D, Mackay G, Kalna G, et al. Improving the metabolic fidelity of cancer models with a physiological cell culture medium. Sci Adv. 2019;5.

65. Jain IH, Calvo SE, Markhard AL, Skinner OS, To T, Ast T, et al. HHS Public Access. 2021;181:716–27.

66. Bao MHR, Yang C, Tse APW, Wei L, Lee D, Zhang MS, et al. Genome-wide CRISPR-Cas9 knockout library screening identified PTPMT1 in cardiolipin synthesis is crucial to survival in hypoxia in liver cancer. Cell Rep. 2021;34:108676.

67. Zhang X, Fryknäs M, Hernlund E, Fayad W, De Milito A, Olofsson MH, et al. Induction of mitochondrial dysfunction as a strategy for targeting tumour cells in metabolically compromised microenvironments. Nat Commun. 2014;5.

68. Palm W, Park Y, Wright K, Pavlova NN, Tuveson DA, Thompson CB. The Utilization of Extracellular Proteins as Nutrients Is Suppressed by mTORC1. Cell. 2015;162:259-70.

69. Hardie DG. AMP-activated protein kinase-an energy sensor that regulates all

aspects of cell function. Genes Dev. 2011;25:1895–908.

70. Young RM, Ackerman D, Quinn ZL, Mancuso A, Gruber M, Liu L, et al. Dysregulated mTORC1 renders cells critically dependent on desaturated lipids for survival under tumor-like stress. Genes Dev. 2013;27:1115–31.

71. Maddocks ODK, Berkers CR, Mason SM, Zheng L, Blyth K., Gottlieb, E, Vousden KH. Serine starvation induces stress and p53 dependent metabolic remodeling in cancer cells. Nature 2019;493:542–6.

72. Eno CO, Zhao G, Olberding KE, Li C. The Bcl-2 proteins Noxa and Bcl-xL co-ordinately regulate oxidative stress-induced apoptosis. Biochem J. 2012;444:69–78.

73. Eichhorn JM, Alford SE, Sakurikar N, Chambers TC. Molecular analysis of functional redundancy among anti-apoptotic Bcl-2 proteins and its role in cancer cell survival. Exp Cell Res. 2014;322:415–24.

74. Hatch H, Dolinski BM, Nguyen T, Harmonay L, Al-Assaad AS, Ayers M, et al. MCL1 and BCL-xL levels in solid tumors are predictive of dinaciclib-induced apoptosis. PLoS One. 2014;9:e108371.

75. Huang DCS, O'Reilly LA, Strasser A, Cory S. The anti-apoptosis function of: Bcl-2 can be genetically separated from its inhibitory effect on cell cycle entry. EMBO J. 1997;16:4628–38.

76. Bonnefoy-Berard N, Aouacheria A, Verschelde C, Quemeneur L, Marçais A, Marvel J. Control of proliferation by Bcl-2 family members. Biochim Biophys Acta - Mol Cell Res. 2004;1644:159–68.

77. D'Aguanno S, Del Bufalo D. Inhibition of Anti-Apoptotic Bcl-2 Proteins in

Preclinical and Clinical Studies: Current Overview in Cancer. Cells. 2020;9.

78. Merino D, Kelly GL, Lessene G, Wei AH, Roberts AW, Strasser A. BH3-Mimetic Drugs: Blazing the Trail for New Cancer Medicines. Cancer Cell 2018;34:879–91.

Figure Legends

Figure 1. An *in vitro* system recapitulates phenotypes associated with hypo-perfused regions of pancreatic tumors

(**A**) Representative confocal images indicating the frequency of proliferating (EdU+, magenta) and apoptotic (CC3+, gray) cells in well perfused and poorly perfused regions in KPCY tumors (Texas-red dextran, red) detected by co-immunofluorescence. Arrows indicate CC3+ apoptotic tumor cells. Scale Bar = 25 μm.

(**B**) Dextran staining was used to distinguish well perfused and poorly perfused regions of the KPCY mice in (**A**) (see Methods). Quantification of the fraction of GFP+ tumor cells that were EdU+ or CC3+ in either region is shown (data pooled from n=3 tumors, 3 sections per tumor and 5 regions per section).

(**C**) 'Fertile' (green) and 'Arid' (orange) culture conditions employed *in vitro*.

(**D**) Representative flow cytometry dot plot and quantification of EdU+ PANC-1 cells following a 24h pulse under fertile conditions or after 7, 14 or 21 days of arid conditions (data pooled from n=3 experiments, 2-3 replicates per experiment).

(**E**) Flow-cytometry based Annexin/PI measurements of PANC-1 cells maintained under fertile and arid conditions (data pooled from n=3 experiments, 2-3 replicates per experiment).

(**F**) Representative histograms and quantification of proliferation kinetics based on PKH26 dilution. The table shows population doubling (PD) times calculated for the various conditions. Data in table represents the mean ± S.E.M. of n=3 experiments, 3 replicates per experiment.

(**G**) Measurement of protein synthesis in PANC-1 tumor cells pulsed with OPP for 1 hour (data pooled from n=3 experiments, 2 replicates per experiment).

(**H**) Measurement of autophagy by quantification of mCherry+/GFP+ ratios of PANC-1 cells expressing the autophagy reporter GFP-mCherry-LC3B (data pooled from n=3 experiments, 2 replicates per experiment).

(**I**) Measurement of macropinocytosis by quantification of intracellular puncta following exposure of PANC-1 cells to TMR-dextran (red) for 30' (data pooled from n=3 experiments, 2 replicates per experiment).

(**J**) Measurement of intracellular ATP levels (per cell) in PANC-1 cells determined by CellTiter-Glo luminescence, normalized to microscopy-based nuclear count (data pooled from n=2 experiments, 4 replicates per experiment).

(**K**) Chemosensitivity analysis of PANC-1 cells treated with the indicated doses of gemcitabine (5d). Viability was determined by comparing nuclear counts at treatment endpoint compared to onset (data pooled from n=2 experiments, 2 replicates per experiment).

In (B,G-I) statistical differences were calculated using unpaired *t* test and in (D) statistical differences were calculated using One-way ANOVA and Dunnett test (comparing to fertile). $P < 0.05$ was considered statistically significant; *, $P < 0.05$; ***, $P < 0.001$ n.s. not significant.

Figure 2. Genome-wide CRISPR screening reveals contrasting dependencies for cells under fertile vs. arid conditions

(**A**) Schematic showing the screening strategy (see text for details).

(**B**) Normalized abundance counts for sgRNAs reflecting essential genes under fertile conditions (depleted in fertile d9 vs. T0 and d30 fertile vs. d9 fertile but not d30 arid vs. d9 fertile).

(**C**) Unfiltered functional annotation by Reactome ($p<0.05$) of sgRNAs depleted in both early (d30 arid vs. d9 fertile) and late exposures (d53 arid vs. d32 fertile) to arid conditions but not fertile conditions (d9 fertile vs. T0, d30 fertile vs. d9 fertile, or d53 fertile vs. d32 fertile).

(**D**) Normalized abundance counts for sgRNAs reflecting essential genes under arid conditions (depleted in d53 arid but not d53 fertile compared to d32 fertile).

(**E**) Drug response curves for CPI-613 and UK-5099 targeting the TCA cycle and MPC1, respectively. Normalized cell counts for cells grown under arid conditions (left vertical axes) vs. fertile conditions (right vertical axes) are different given the slow cycling nature of the former and the rapidly proliferating status of the latter (datapoints are the means of n=2 experiments).

(**F**) Unfiltered functional annotation by Biocarta ($FC>1.33$, $p<0.05$) of sgRNAs enriched under arid conditions (d30 arid vs. d9 fertile and but not d30 fertile vs. d9 fertile).

(**G-H**) Quantification of DNA synthesis by EdU incorporation (**G**) and protein synthesis by OPP incorporation (**H**) after 7 days of arid conditions, comparing sgTSC2 to control (EV). EdU data pooled from n=3 experiments, 2 replicates; OPP data pooled from n=2 experiments, 2 replicates each.

(**I**) Immunoblot of total S6 and phospho-S6 levels in control PANC-1 cells (EV) or cells lacking TSC2 (sgTSC2) following 3 days under arid conditions.

(**J**) Results of competition between EV-GFP cells and mcherry-sgTSC2 cells, with samples collected at the indicated timepoints (data pooled from n=3 experiments, 2 replicates per experiment).

In (G) statistical differences were calculated using *t* test. In (J), statistical differences were calculated using multiple *t* tests. $P < 0.05$ was considered statistically significant; *, $P < 0.05$; **, $P < 0.01$.

Figure 3. Bcl-xL is essential and non-redundant under arid conditions.

(**A**) Dot plot showing log-fold change in sgRNA abundance (each dot represents the pool of sgRNAs targeting a single gene) of cells maintained in fertile conditions (X-axis) or switched to arid conditions (Y-axis) at early (left panel) and late (right panel) timepoints of the CRISPR screen. The adjusted p-values for Bcl-xL (BCL2L1, red) are $1.81\text{^}10^{-6}$ and $1.17\text{^}10^{-5}$ respectively. Other Bcl-2 family members did not show a significant change and are highlighted (blue).

(**B**) Western blots showing the expression of Bcl-xL and Mcl-1 under fertile and arid conditions.

(**C**) Results of competition between EV-GFP and Bcl-xL KO-mCherry PANC-1 clones grown under fertile or arid conditions for the indicated times (data pooled from n=3 experiments, 2-3 replicates per experiment).

(**D**) Results of competition in a panel of human and mouse cell lines lacking Bcl-xL under fertile and arid conditions (data pooled from n=2 experiments, 1-2 replicates per experiment). Cells were sampled at different timepoints according to their survival capacity under arid conditions. AsPC-1 (3d), HPAC (7d), BxPC3 (7d) and MH6620c1 (14d).

(**E**) Quantification of non-viable cells in EV and Bcl-xL KO PANC-1 clones following transfer to arid conditions, determined by flow cytometry for Annexin V and DAPI (data pooled from n=3 experiments, 2-3 replicates per experiment).

(**F**) Dose response of PANC-1 cells treated with Bcl-xL inhibitor A-1155463 for 4 days. Cells were grown in either fertile conditions throughout (“Fertile”), transferred to arid conditions at the onset of treatment (“Acute”) or pre-acclimated to arid conditions for 14

1229 days before treatment began ("Chronic"). Cell numbers are plotted relative to cell
1230 number at the beginning of treatment and are the means of n=2 experiments.
1231 (**G**) Results of competition between EV and Bcl-xL KO-mCherry PANC-1 clones
1232 following addback of various nutrients in the presence of 1% O_2 (data pooled from n=3
1233 experiments, 2 replicates per experiment).
1234 In (C,E,G) statistical differences were calculated using One-way ANOVA and Dunnett
1235 test (Comparing to d0 (C), EV (E) and baseline arid (G). In (D), statistical differences
1236 were calculated using *t* tests. For panel (G), significance is indicated relative to baseline
1237 (arid) conditions). $P < 0.05$ was considered statistically significant; *, $P < 0.05$; **, $P <$
1238 0.01. ***, $P < 0.001$. n.s.-not significant.
1239

Figure 4. Bcl-xL is necessary for survival of quiescent PDAC cells *in vivo.*

(**A**) Measurement of median tumor volumes comparing subcutaneously implanted EV and Bcl-xL KO tumor clones (n=8 EV; n=6 Bcl-xL KO1; n=6 Bcl-xL KO2).

(**B-C**) Measurements of tumor weight (**B**), and apoptotic rate (**C**) in tumors shown in (**A**).

(**D**) Representative confocal image and image-based quantification of EV (green) and Bcl-xL KO (red) mixed tumors. Dashed line approximates well perfused (left) and poorly perfused (right) regions for illustration purposes. Scale bar=100 μm.

(**E**) Measurement of the area occupied by Bcl-xL KO-mCherry cancer cells and EV-GFP tumor cells in mixed tumors (n=5).

(**F**) Ratio between EV-GFP and Bcl-xL KO-mCherry cells as a function of distance from dextran-positive perfused regions in mixed tumors (n=5).

(**G**) Quantification of the spatial distribution of cleaved caspase-3+ cancer cells in PANC1-GFP xenografts injected intratumorally with A-1155463 or vehicle (n=5).

(**H**) Quantification of the spatial distribution of cleaved caspase-3+ cancer cells in PANC1-GFP xenografts injected with Gemcitabine/Nab-Paclitaxel or PBS (n=5).

(**I**) Top: Schematic of the experimental strategy for combining Gemcitabine and Nab-paclitaxel (Gem/nP) with the Bcl-xL inhibitor A-1331852. Bottom: Waterfall plots showing final change in the volume of MH6620c1 tumors grown in immunocompetent C57Bl/6 hosts following 14 days of treatment.

In (A) statistical differences were calculated using repeated measures One-way ANOVA and Dunnett test (Compared to EV), In (B,C) statistical differences were calculated using One-way ANOVA and Dunnett test (Comparing to EV) and in (E,G,H) statistical

differences were calculated using *t* tests. $P < 0.05$ was considered statistically significant; *, $P < 0.05$; ***, $P < 0.001$.

Figure 5. Quiescent cells in human PDAC exhibit signatures of nutrient and oxygen deprivation.

(**A**) Relative abundance of Bcl-xL mRNA across tumor types from TCGA data.

(**B**) Relative abundance of Bcl-xL mRNA comparing PDAC and normal pancreas tissue (TCGA).

(**C**) Correlation (hazard ratio) between Bcl-xL mRNA levels and patient survival across The Cancer Genome Atlas (TCGA).

(**D**) Kaplan-Meier plot showing PDAC survival based on the top (red) and bottom (blue) quartiles of BCL2L1 in PDAC (TCGA).

(**E**) Top: UMAP plots of single cell RNA-sequencing profiles from 3 independent studies of human PDAC. The proliferative subpopulation of tumor cells is shown in green, and the quiescent subpopulation of tumor cells is shown in orange. Bottom: Relative expression of BCL2L1 and cell cycle markers segregated into proliferative and quiescent subpopulations. Panels represent pooled data pooled from n=24 (Peng et al.), n=10 (Steele et al.), and n=16 (Lin et al.) tumors, respectively.

(**F**) Functional annotation by GSEA msGDMIB for Hallmark pathways of upregulated and downregulated genes, comparing quiescent cells to proliferating cells in data from Peng et al. (FDR<0.05).

Figure 6. Bcl-xL protects cells from "inappropriate" biosynthesis

(**A**) Functional annotation by GSEA Hallmark pathways of genes upregulated or downregulated in Bcl-xL KO clones comparing to EV cells under arid conditions (FDR<0.05).

(**B**) Western blots of c-Myc and S6 phosphorylation under fertile and arid conditions in EV and Bcl-Xl KO cells.

(**C**) Flow cytometry-based measurements of EdU+ cells in EV and Bcl-xL KO clones (24h pulse) during the first 3 days in arid conditions (data pooled from n=3 experiments, 2 replicates per experiment).

(**D**) Immunostaining-based quantification of Ki-67+ cells in cells cultured at day 7 under arid condition. (n=3).

(**E**) Schematicsdepicting cell cycle phase marking by the FUCCI-PIP reporter.

(**F-H**) Frequency of G1→S transitions (F) frequency of mitotic events (G) and frequency of cell death in G1, S and G2 (H) comparing control (EV) and Bcl-xL KO (non-clonal) cells tagged with FUCCI-PIP over 48hrs of timelapse microscopy starting at 2 days of arid culture. Results represent the mean of at least 3 different fields over two-three separate sessions. (Abemacicilib, Abm).

(**I**) Representative confocal images and histogram showing frequency of Ki-67+ tumor cells as a function of distance from perfused blood vessels in EV-GFP (n=3) and Bcl-xL KO1-mCherry (n=4) PANC-1 cells derived xenografts. Scale Bar = 100 μm.

In (C,D, F-H) statistical differences were calculated using One-way ANOVA and Dunnett test (Compared to EV) . $P < 0.05$ was considered statistically significant; *, $P < 0.05$; **, $P< 0.01$. ***, $P< 0.001$. ****, $P< 0.0001$.

Figure 7. Biosynthetic pressure under nutrient deprivation is lethal to genetically intact PDAC cells

(**A-B**) Fraction of EdU+ (**A**) or non-viable (**B**) PANC-1 cells cultured under arid conditions for 72h with an addback of serum and/or glucose (data pooled from n=3-4 experiments, 2-3 replicates per experiment).

(**C-D**) Fraction of EdU+ (**C**) or non-viable (**D**) PANC-1 cells cultured under arid conditions for 72h with an addback of serum in the presence or absence of the indicated biosynthesis inhibitors (data pooled from n=2-5 experiments, 2-3 replicates per experiment).

Statistical differences were calculated using One-way ANOVA and Sidak test. $P < 0.05$ was considered statistically significant; *, $P < 0.05$; **, $P< 0.01$. ***, $P< 0.001$. n.s.-not significant.

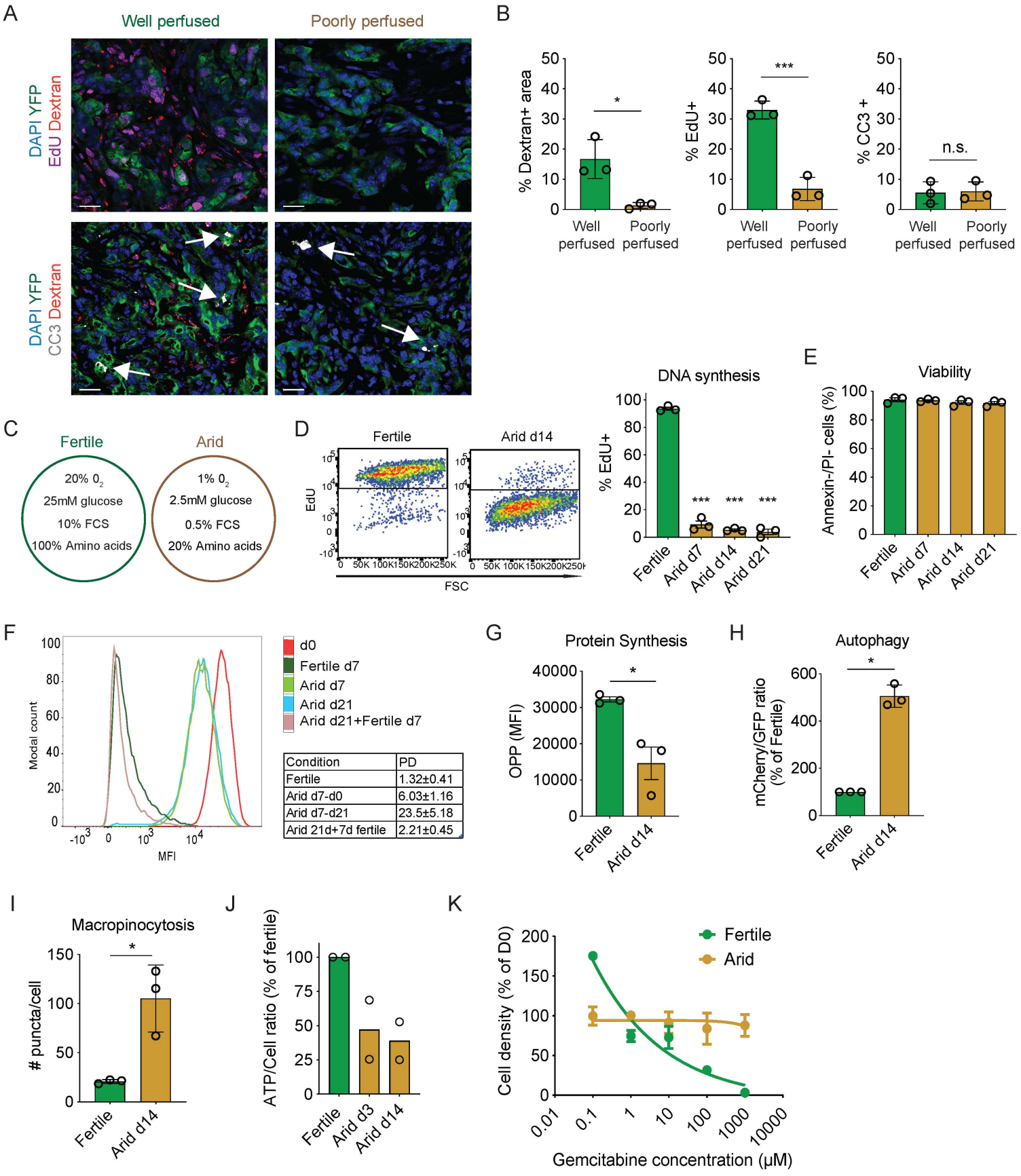

Figure.1

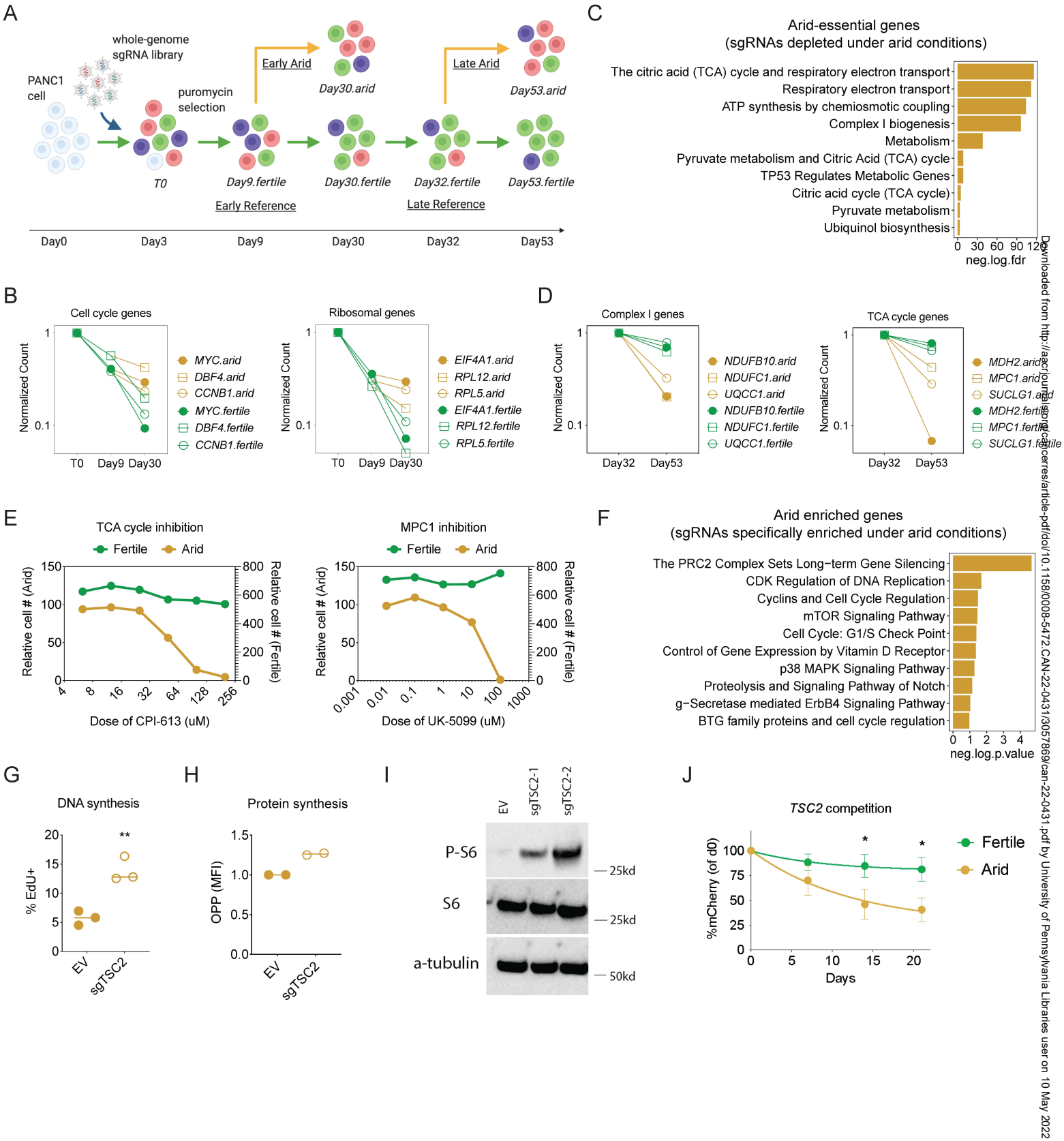

Figure.2

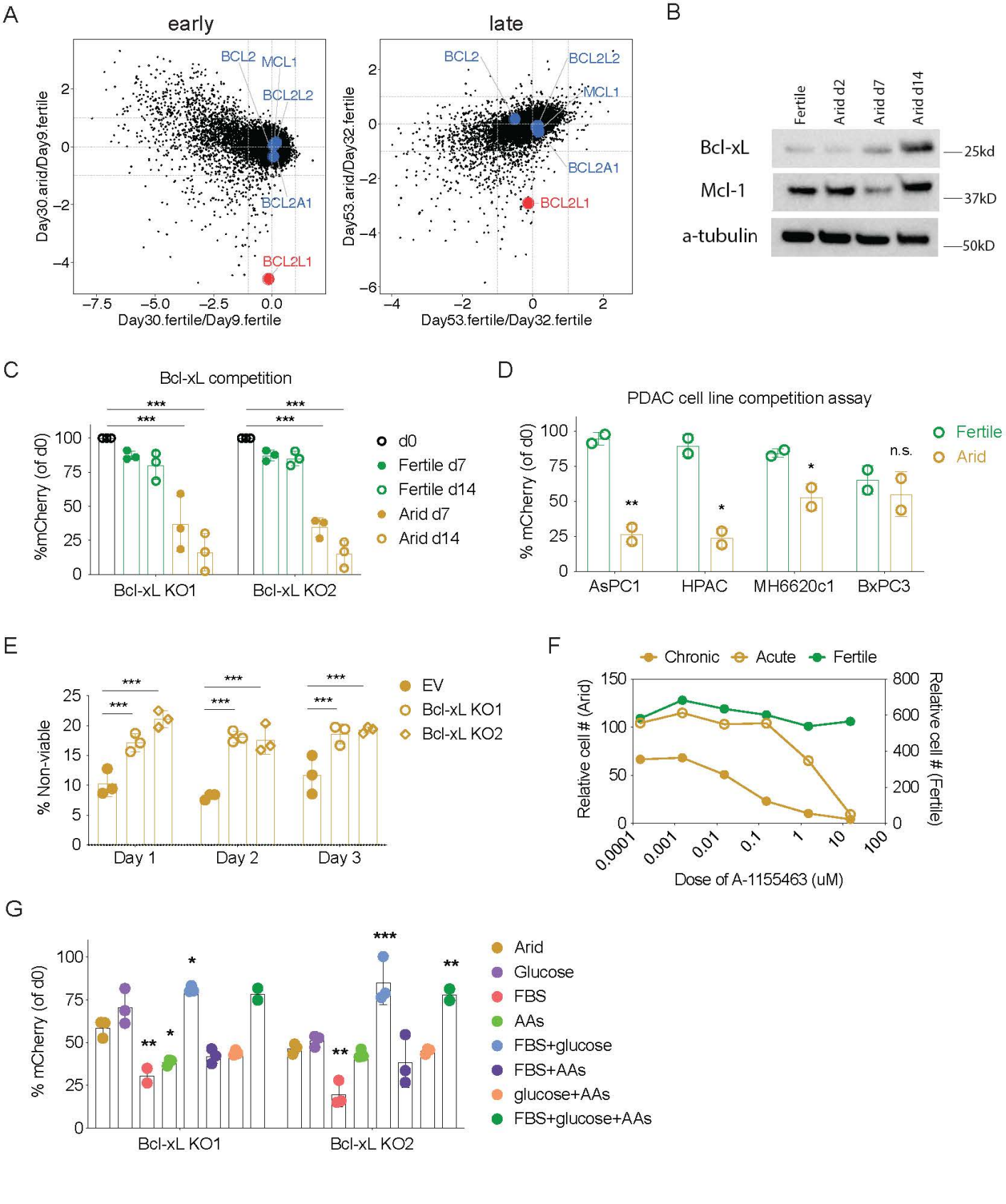

Figure.3

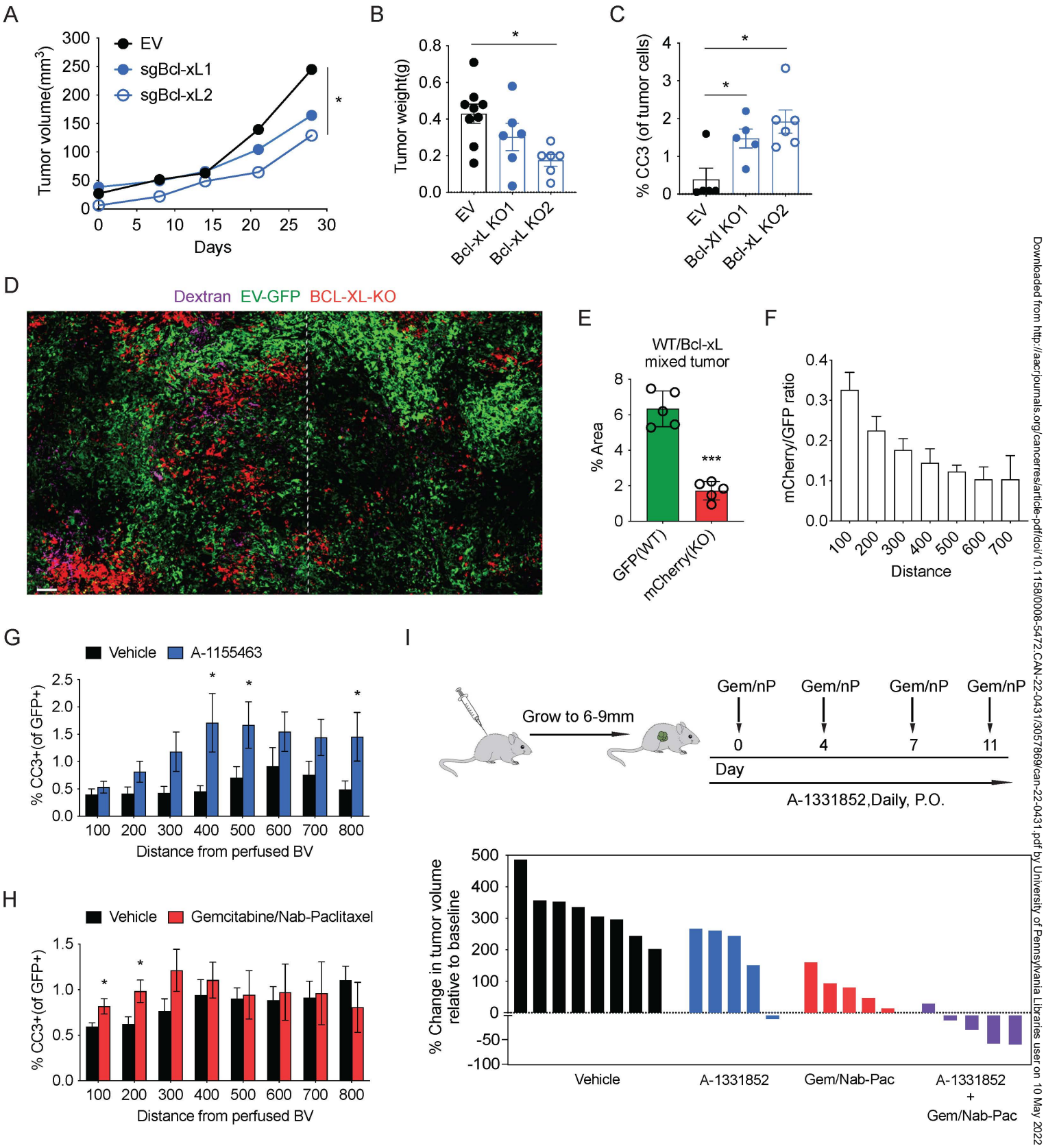

Figure.4

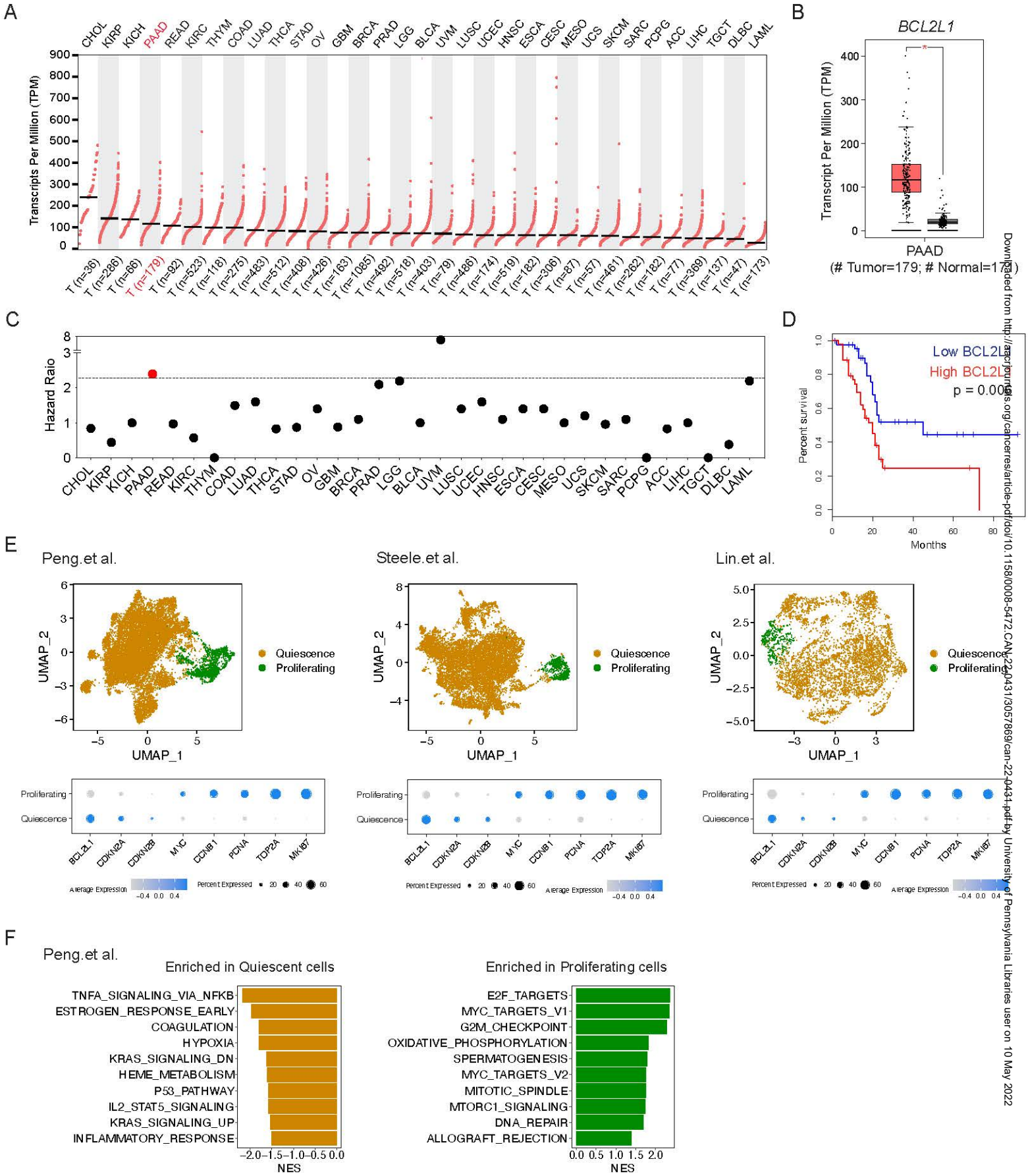

Figure.5

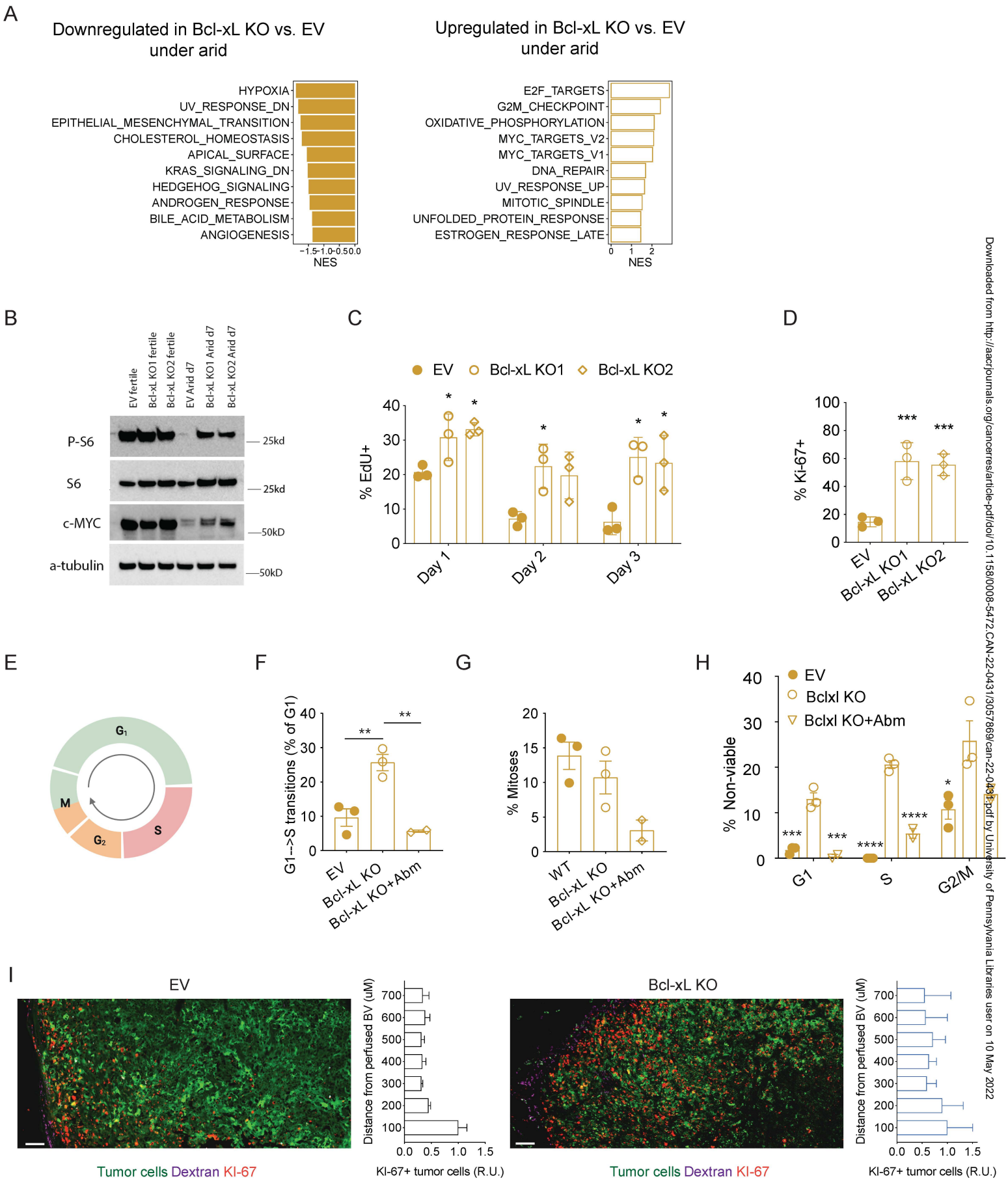

Figure.6

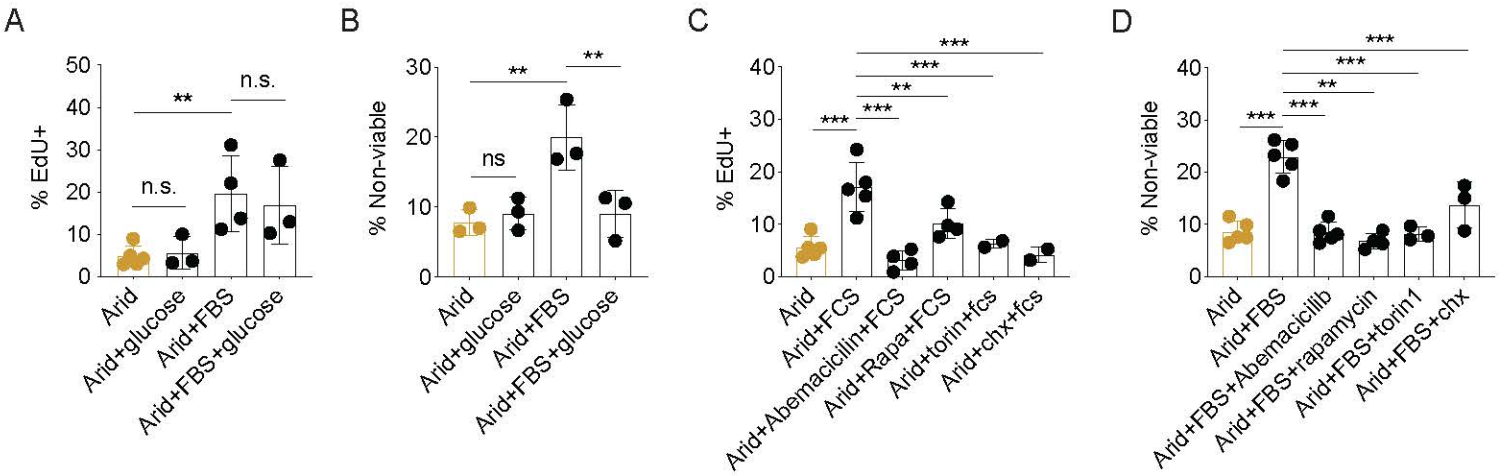

Figure.7